



Norwegian University of
Science and Technology

Micromagnetic Modelling of Thermally Induced Errors in Nanomagnetic Logic

Hanna Heggheim Lee

Nanotechnology

Submission date: January 2018

Supervisor: Erik Folven, IES

Co-supervisor: Einar Standal Digernes, IES

Norwegian University of Science and Technology
Department of Electronic Systems

Abstract

Micromagnetic simulations have been used to study nanomagnet structures of $\text{La}_{0.7}\text{Sr}_{0.3}\text{MnO}_3$ (LSMO) with the aim of use in nanomagnetic logic (NML). Studying the success rate of signal propagation in chains of nanomagnets has been the main focus of this work and different system parameters have been investigated; aspect ratio of the magnets, intermagnet spacing, thickness and uniaxial anisotropy. The success rate has been shown to increase with increasing thickness, decreasing intermagnet spacing, and by adding a uniaxial anisotropy term along the shape anisotropy hard axis of the magnets.

In addition to investigating signal propagation in horizontally aligned nanomagnet chains, fanout structures including both horizontal and vertical nanomagnet chains have been studied. Even though successful propagation was not observed for this NML structure, insight was gained in the challenges of signal propagation in a larger circuit. From the results obtained here, suggestions are made regarding which system parameters should be explored as a next step towards successfully building more complex NML systems.

Samandrag

Mikromagnetiske simuleringar har vorte nytta til å studere nanomagnetstrukturar av $\text{La}_{0.7}\text{Sr}_{0.3}\text{MnO}_3$ (LSMO), med mål om bruk i nanomagnetisk logikk (NML). Å studere suksessraten til signalpropagering i nanomagnetkjeder har vore hovudfokus i dette arbeidet. Systemparametrar som har vorte utforska er nanomagnetdimensjonar, tjukkeleik, avstand mellom magnetane og uniaksial anisotropi. Suksessraten har vist seg å auke med aukande tjukkeleik, minkande avstand mellom magnetane og ved å leggje til uniaksial anisotropi langs kortsida til magnetane (i planet).

I tillegg til å utforske signalpropagering i horisontalt opplinjerte nanomagnetkjeder, har ein fanoutstruktur med båe horisontale og vertikale nanomagnetkjeder vorte studert. Sjølv om suksessfull propagering ikkje vart observert for denne NML-strukturen, fekk me innsikt i utfordringane ved signalpropagering i ein større krins. Med utgangspunkt i resultata frå desse simuleringane vert det lagt fram forslag til kva for nokre systemparametrar som burde utforskast som neste steg på vegen mot å lage meir komplekse NML-system.

Preface

This master's thesis is the final part of my Master of Science degree in Nanotechnology at the Norwegian University of Science and Technology (NTNU). The work presented here was conducted in the fall of 2017 for the oxide electronics group at the Department of Electronic Systems at NTNU. It is a continuation of my specialization project, which was carried out in the spring of 2017. Parts of the chapters on theory and model system have been reused and improved from the specialization project report.

I want to extend my gratitude to my supervisor Assoc. Prof. Erik Folven and co-advisor Einar Standal Digernes for mentoring me with great enthusiasm, and to Sam Slöetjes for answering all of my simulation related questions. Thank you to my family for always being supportive. Additionally, a big thank you to all the people who have made my time as a student in Trondheim so memorable. It's been a blast!

Hanna Heggheim Lee

Trondheim, January 2018

Contents

1	Introduction	1
1.1	Motivation	1
1.2	Project outline	2
2	Theory	3
2.1	Ferromagnetism	3
2.2	Micromagnetics	7
2.3	Boolean logic	9
2.4	Nanomagnetic logic	11
3	Model System and Simulation Procedures	17
3.1	Model system	17
3.2	MuMax3	19
3.3	Material parameters	21
3.4	Simulation procedures	24
3.4.1	Nanomagnet chains	24
3.4.2	Nanomagnet fanout structure	29
4	Results and Discussion	31
4.1	Nanomagnet chains	31
4.1.1	Nanomagnet dimensions	32
4.1.2	Thickness	34
4.1.3	Intermagnet spacing	35
4.1.4	Uniaxial anisotropy	38
4.1.5	Findings for the nanomagnet chains	43
4.2	Nanomagnet fanout structure	44

4.2.1 Findings for the fanout structure	46
5 Conclusions and Outlook	49
A Simulation Scripts	51
References	57

Chapter 1

Introduction

1.1 Motivation

Proposed by Intel co-founder Gordon Moore in 1965, Moore's law states that the number of transistors on an integrated circuit will approximately double every 24 months [1, 2]. The semiconductor industry has long used Moore's law as a guide for the scaling of transistor technology. However, at the time of writing, Moore's law seems to have come to a halt. Intel's next transistor technology, the Cannon Lake 10 nm technology, was originally scheduled to arrive in January of 2016. It has since been pushed back three times, and is at the time of writing scheduled for late 2018 [3]. With the time scale of Moore's law no longer keeping pace with the predictions, many have declared the end of Moore's law, and a new approach to advances in semiconductor industry has emerged, termed "More than Moore". The focus has shifted from increasing transistor density to manufacturing highly integrated chips [4].

Intel predicts that the semiconductor industry will be unable to continue the downscaling of silicon transistors in five years [5]. Spintronics, which utilizes the electron spin instead of the charge, is a promising beyond-CMOS technology. One of the candidates for a spintronic implementation is nanomagnetic logic (NML). This technology, which is based on signal propagation in chains of bistable nanomagnets, has the potential to offer dense, non-volatile devices with low power consumption [6].

It is possible to make nanoscale magnets which comprise only a single domain. Magnetic anisotropy can give rise to a bistable situation where two orientations of this domain is

energetically favorable. Thus, a system that is well suited to represent the binary states 0 and 1. In in-plane nanomagnetic logic (iNML), the energetically favorable magnetization states point along the longest dimension of the magnets. Signal propagation in a chain of nanomagnets is made possible by exploiting the interactions between adjacent nanomagnets together with the magnets' bistability.

A transition from today's charge based logic to spin based logic could provide a viable route for continued improvement of computational functionality beyond CMOS. However, some challenges must be addressed before the shift can be made. One of the main challenges NML is faced with is high error rates, especially for room temperature operation.

1.2 Project outline

Nanomagnet structures of $\text{La}_{0.7}\text{Sr}_{0.3}\text{MnO}_3$ (LSMO) have been investigated with the aim of use in NML. Some of the materials which have commonly been studied for NML application are permalloy [7, 8, 9] and supermalloy [10, 11]. Due to its biaxial magnetocrystalline anisotropy, LSMO serves as a promising material for NML devices. The material is extensively studied in the oxide electronics group at NTNU [12, 13, 14], where it is grown with pulsed laser deposition. The micromagnetic simulation tool MuMax3 [15] has been used to investigate the behavior of systems of LSMO nanomagnets. The results from this thesis can contribute in the fabrication process of the LSMO magnets by highlighting material parameters which can contribute to finding viable nanomagnetic systems.

Chapter 2 presents the theoretical foundation. The model system and simulation procedures are described in chapter 3, followed by chapter 4 presenting results and discussion. In chapter 5 the findings are summarized and suggestions for further work are made. Two representative scripts used for the simulations can be found in appendix A.

Chapter 2

Theory

This chapter gives an overview of the theoretical background for the work that has been carried out. Ferromagnetism is the first topic presented, in section 2.1. The micromagnetic model is covered in section 2.2. Section 2.3 deals with the fundamentals of logic. The specific case of nanomagnetic logic is presented in section 2.4.

2.1 Ferromagnetism

A ferromagnetic material is characterized by the ability of having a spontaneous net magnetization (i.e., in the absence of a magnetic field) below a characteristic temperature, T_c , known as the Curie temperature. Figure 2.1 shows a ferromagnetic material which is divided into several domains. Each domain is a region of the material where all the electron spins align, i.e., a region of uniform magnetization. The local spin alignment is attributed to the exchange coupling, a quantum mechanical effect which governs the interactions between magnetic atoms or ions. In a ferromagnetic material, the exchange energy will be minimized by aligning neighboring spins.

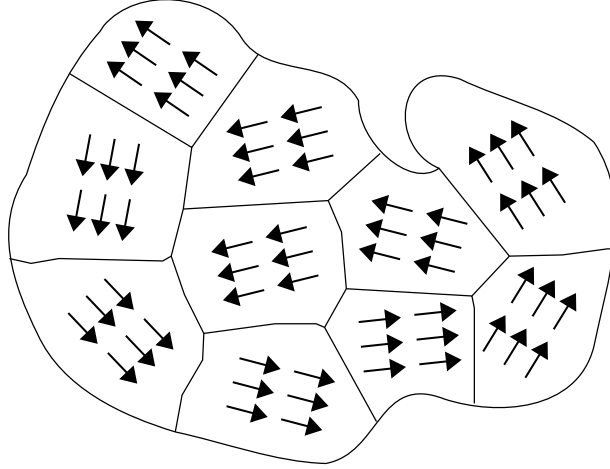


Figure 2.1: Schematic of a ferromagnetic material subdivided in regions of uniform magnetization, referred to as magnetic domains.

The Stoner criterion predicts which metals are ferromagnetic materials, and is given by

$$U_g(E_F) > 1. \quad (2.1)$$

The property $U_g(E_F)$ depends on the electronic density of states at the Fermi level, E_F , and a material dependent factor describing the exchange interaction [16]. The criterion successfully predicts the transition metals Fe, Co and Ni to be ferromagnetic. However, the model works best for elemental materials, in addition to inferring too high Curie temperatures [17].

Applying an external magnetic field to a ferromagnetic material will cause the magnetic domains to align along the magnetic field direction and lead to an increase in the magnetization of the material. Above the Curie temperature, the thermal energy overcomes the exchange energy. The material becomes paramagnetic; it will only exhibit a net magnetization in the presence of a magnetic field.

An important energy contribution in a ferromagnetic system is the demagnetization energy. Demagnetizing fields are magnetic field which form to counteract the magnetization of the material, reducing the total magnetic moment. Figure 2.2 demonstrates that domain formation is a result of minimizing the demagnetization energy. The leftmost magnet consists of only one domain. Since there is long-range ordering of the spins, the exchange energy is low. Having only one domain, the demagnetizing field is large. Hence, the demagnetization energy of the magnet has a considerable contribution to the total energy

of the system. The magnet in the middle is divided into two domains, reducing the demagnetizing field and increasing the exchange energy. The demagnetization energy is further reduced by the four domains of the rightmost magnet. Domain formation reduces the demagnetization energy at the expense of increasing the exchange energy.

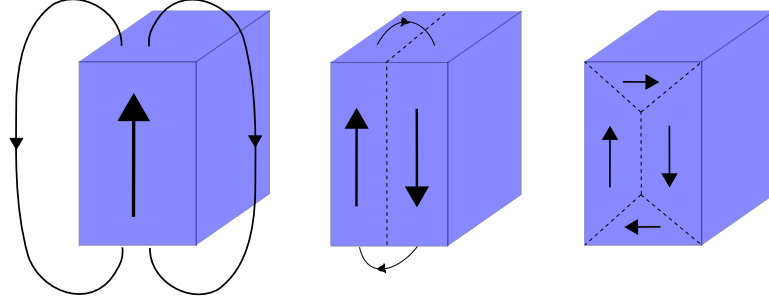


Figure 2.2: An illustration of how the formation of magnetic domains will reduce the stray fields.

Another interesting feature of ferromagnetic materials is hysteresis. Applying and removing a magnetic field will leave the material in a different magnetization state than the initial state. Figure 2.3 shows a hysteresis loop with the magnetic field, \vec{H} , along the x-axis and the magnetization, \vec{M} , along the y-axis.

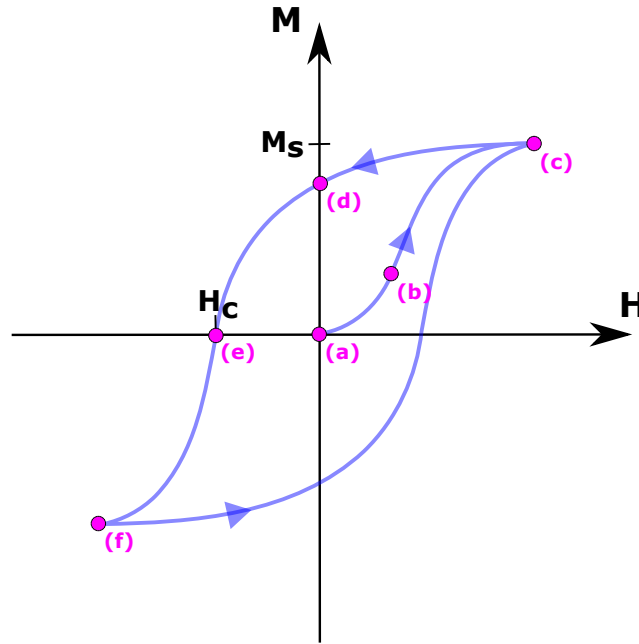


Figure 2.3: A hysteresis loop showing how the magnetization, \vec{M} , of a ferromagnetic material responds to the application of a magnetic field, \vec{H} .

The subfigures of figure 2.4 qualitatively demonstrate the effect of exposing a ferromagnetic material to a magnetic field. At point (a) of the hysteresis loop, the magnetization directions of the domains cancel out overall, as seen in figure 2.4a. From the demagnetized state a magnetic field is applied. As the magnetic field strength is increased, the domains start to align along the magnetic field direction. Figure 2.4b shows the state at point (b). Some of the domains have started aligning their magnetic moment along the field direction. The magnetic field has induced a net magnetization in the ferromagnet. The curve in figure 2.3 flattens at point (c) when further increasing the magnetic field does not lead to a considerable increase in the magnetization. The magnetization at this point is called the saturation magnetization, M_s . All of the domains in figure 2.4c are magnetized along the magnetic field.

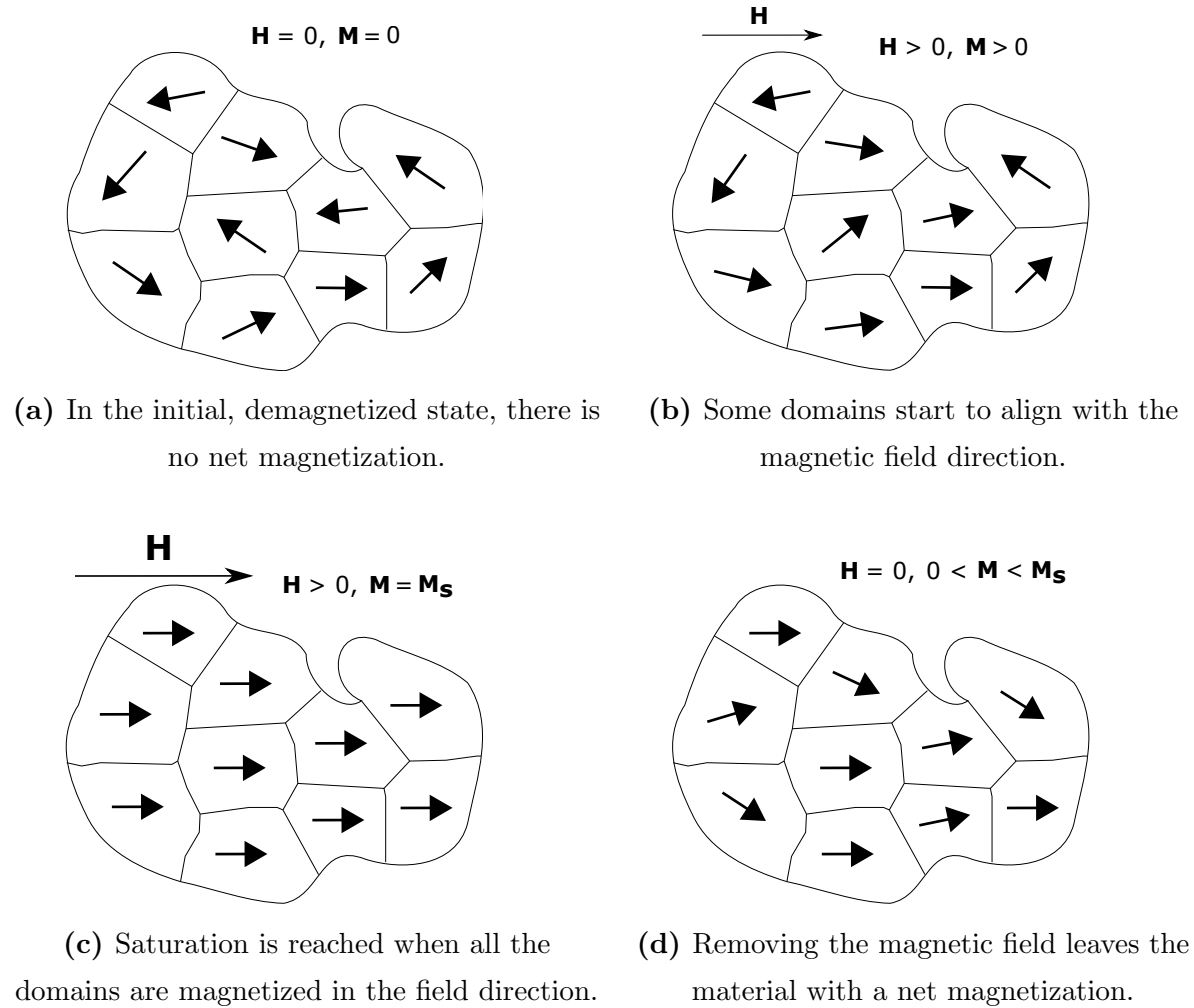


Figure 2.4: The subfigures (a) to (d) show the magnetization states of domains in a ferromagnetic material upon the application and removal of a magnetic field.

Turning off the magnetic field renders the material in a different magnetization state than prior to the exposure. At point (d), the material still has a net magnetization, as seen in figure 2.4d. The magnetization remaining after removing the magnetic field is called the remanent magnetization. In order to further reduce the magnetization, a magnetic field must be applied in the opposite direction to the initial field. The field necessary to return the material to a state of $M = 0$ at point (e) is called the coercive field, \vec{H}_c . Increasing the strength of the magnetic field further will lead to saturation at point (f), again with domains being magnetized along the magnetic field direction.

2.2 Micromagnetics

Micromagnetics is a field in physics which deals with ferromagnetism in nano and micro structures. The magnetic ground state of a system is calculated by utilizing a method of energy minimization. Because the micromagnetic model combines classical physics and quantum mechanics, it is a semiclassical model. For example, the magnetization of a material is modelled as a continuous property, but interactions between electrons are still taken into account.

Based on Weiß' work on domain formation in ferromagnetic materials [18], Landau and Lifshitz initiated the scientific field of micromagnetics in 1935 [19]. The first micromagnetic model was restricted to one dimension. One of the weaknesses of the initial model was that only short-range interactions were taken into account, largely ignoring magnetostatic interactions. A complete 3D model was developed by Brown, wherein the magnetostatic interactions were properly accounted for [20, 21]. The model was published in 1963.

The Landau-Lifshitz differential equation is the fundamental equation governing micromagnetics:

$$\frac{\partial \vec{M}}{\partial t} = \lambda_1 \vec{M} \times \vec{H}_{eff} - \lambda_2 \vec{M} \times (\vec{M} \times \vec{H}_{eff}), \quad (2.2)$$

where \vec{M} is the magnetization, \vec{H}_{eff} is the effective magnetic field strength and λ_1 and λ_2 are constants where $\lambda_2 > 0$ [18]. \vec{H}_{eff} is the effective magnetic field. It is defined as:

$$\vec{H}_{eff} = -\frac{\partial}{\partial \vec{M}} \mathcal{E}_{mag}(\vec{M}), \quad (2.3)$$

where \mathcal{E}_{mag} is the density of the total magnetic energy. The effective magnetic field has contributions which are determined by the energy contributions of the system.

\vec{m} is called the reduced magnetization and is a normalization of the total magnetization, \vec{M} . \vec{m} is found by dividing \vec{M} by the saturation magnetization, M_s :

$$\vec{m} = \frac{\vec{M}}{M_s}. \quad (2.4)$$

The micromagnetic method of finding the reduced magnetization is to minimize the magnetic energy of the system by numerically solving the Landau-Lifshitz differential equation (equation 2.2).

The total energy has five contributions:

- The demagnetization energy, E_{demag} , which arises due to the demagnetizing field. Minimizing the demagnetization energy, i.e., making the demagnetizing field weaker, can be done by domain formation. Also, the demagnetization energy will be minimized by aligning the magnetization direction with the longest dimension of the sample. This effect is often referred to as shape anisotropy, but is in reality mainly a result of reducing the demagnetization energy.
- The magnetocrystalline anisotropy energy, E_{anis} . Crystalline ferromagnetic materials may favor magnetization along certain crystalline directions. These directions are referred to as easy axes and the magnetocrystalline energy is minimized when the magnetization is along either of these. Crystalline directions in between the easy axes give rise to maximal magnetocrystalline energy and are referred to as hard axes. Two examples of crystal anisotropy is uniaxial and biaxial anisotropy, which have one and two favored magnetization directions, respectively.
- The exchange energy, E_{exch} , is related to the exchange coupling, the quantum mechanical effect which favors a parallel configuration of electron spins in ferromagnetic materials. The exchange energy is thus minimized by having all spins pointing in the same direction, forming a single domain.
- The thermal energy, $E_{thermal}$, which is linearly dependent on the temperature. Increasing the temperature induces more lattice vibrations and a higher thermal energy. The energy term is minimized at zero temperature, where the particles in the material have minimal motion.
- The Zeeman energy, E_{Zeeman} , also called the external field energy. It comes into play if an external magnetic field is applied. The Zeeman energy is minimized when the magnetic moments in the material align with the applied magnetic field.

There are two methods for calculating the magnetization; the finite-difference method and the finite-element method. The finite-difference method offers better performance than the finite-element method. However, the finite-element method is better suited for modelling complex geometric structures [15].

As discussed in section 2.1, domains arise as a result of competition between minimizing the demagnetization energy and the exchange energy. The magnetic exchange length, l_{ex} , is a measure for the relative strength between these two energies [22]. For dimensions smaller than l_{ex} , the exchange coupling dominates and spins are aligned in parallel, forming a monodomain configuration. The exchange length is given by

$$l_{ex} = \sqrt{\frac{2A_{ex}}{\mu_0 M_s^2}}, \quad (2.5)$$

where A_{ex} is a material specific parameter called the exchange constant or the exchange stiffness, μ_0 is the permeability of vacuum and M_s is the saturation magnetization [22].

2.3 Boolean logic

Boolean logic plays a fundamental role in modern computing. Its values are the binary values 1 and 0, or "true" and "false". Together with the three fundamental logical operators NOT, AND and OR, the logical values form the basis for logic processing in digital electronics. Logic gates are devices that implement logical functions. The output from the gate, Q , is based on the input values, A and B , and the logical function of the gate. Table 2.1 shows the logic gates and their functions. The NOT gate takes only one input and simply inverts it, i.e., if the input is 0, the output is 1. The other gates all have two inputs. The output of the AND gate is 1 if both the inputs are 1, and 0 otherwise. The OR gate outputs 0 if both of the inputs are 0, and 1 otherwise. Combining multiple logic gates allows for engineering of complex digital systems.

Table 2.1: An overview of the logic gates, their Boolean expressions and truth tables.

Logic gate	Boolean expression	Truth table		
NOT	$Q = \overline{A}$		A	Q
			0	1
			1	0
AND	$Q = A \cdot B$	A	B	Q
		0	0	0
		0	1	0
		1	0	0
		1	1	1
OR	$Q = A + B$	A	B	Q
		0	0	0
		0	1	1
		1	0	1
		1	1	1
NAND	$Q = \overline{A \cdot B}$	A	B	Q
		0	0	1
		0	1	1
		1	0	1
		1	1	0
NOR	$Q = \overline{A + B}$	A	B	Q
		0	0	1
		0	1	0
		1	0	0
		1	1	0
XOR	$Q = A \oplus B$	A	B	Q
		0	0	0
		0	1	1
		1	0	1
		1	1	0

Continued on next page

Table 2.1 – *Continued from previous page*

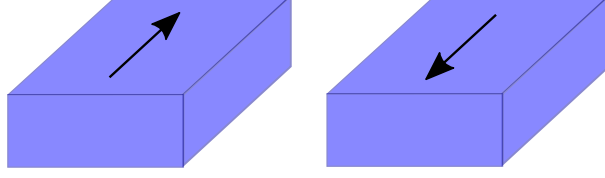
Logic gate	Boolean expression	Truth table		
XNOR	$Q = \overline{A} \oplus \overline{B}$	A	B	Q
		0	0	1
		0	1	0
		1	0	0
		1	1	1

2.4 Nanomagnetic logic

Nanomagnetic logic (NML) is based on chains of bistable nanomagnets, usually of elliptical or rectangular geometry. Normally, the energy cost of the demagnetizing field favors domain formation. However, when the dimensions of the magnet are in the nano range, the magnet is small enough that it is energetically favorable to have a monodomain state, which is paramount for use in logic [23, p. 1011]. Magnets used in NML have two stable magnetization states which represent the binary states 0 and 1 used in Boolean logic, presented in section 2.3.

There are two implementations of nanomagnetic logic; in-plane NML (iNML) and perpendicular NML (pNML), the main difference being the orientation of the stable states. The stable states for both systems are shown in figure 2.5. In iNML the magnets are stable when the magnetization direction is along the longest dimension of the magnet, in the plane. pNML is characterized by having the binary states pointing out of the plane, perpendicularly. Throughout this section, iNML will be used to demonstrate the concept of nanomagnetic logic.

iNML



pNML

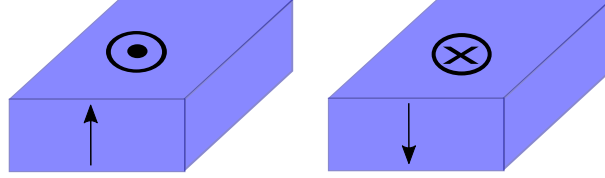


Figure 2.5: An illustration of the two implementations of nanomagnetic logic; in-plane NML (iNML) and perpendicular NML (pNML), and their two stable magnetic states.

The longest in-plane dimension is a shape-induced easy axis; the two favored magnetization directions align with the axis due to shape anisotropy. There are two ways of positioning the nanomagnets when forming a chain; short-side to short-side or long-side to long-side. The most common configuration is the latter, which exploits the antiferromagnetically ordered ground state of a chain of nanomagnets, which was first demonstrated by Cowburn *et al.* in 2002 [24]. The short-side to short-side setup favors a ferromagnetic ordering of the magnetization states.

Logic propagation over a chain of magnets is possible due to interactions between the demagnetizing fields of adjacent magnets. The chain is normally initialized by applying a magnetic field (clocking field) in the direction of the shape anisotropy hard axis of the magnets, i.e., along the smallest in-plane dimension. When magnetized along the hard axis, a single magnet will be in an unstable energy state. However, when inserted into a chain, the magnet will experience hard axis stabilization due to the demagnetizing fields of

nearby magnets [25]. Figure 2.6 shows an NML chain stabilized along its shape anisotropy hard axis. An input magnet is placed in the upper left corner and a stabilizer magnet is positioned at the end of the chain.

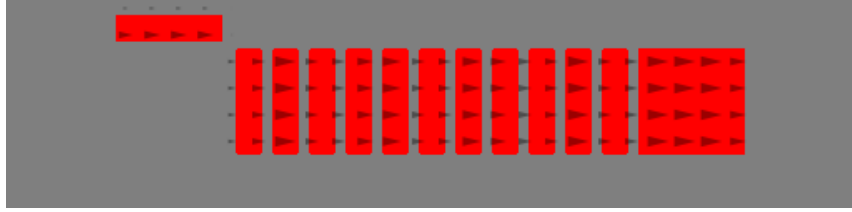


Figure 2.6: Hard axis stabilization of a nanomagnet chain after applying a clocking field in the $+x$ -direction.

Signal propagation can be initiated by placing an input magnet at the start of the chain, 90° rotated compared to the chain magnets, and placed so that its demagnetizing field acts on the first magnet in the chain. Upon removal of the clocking field, the input magnet (being magnetized along its easy axis) is able to provoke a switching of the magnetization of the first magnet in the chain to one of the stable states, with magnetization upwards or downwards. Figure 2.7 shows how the input magnet induces switching of the first magnet in the chain.

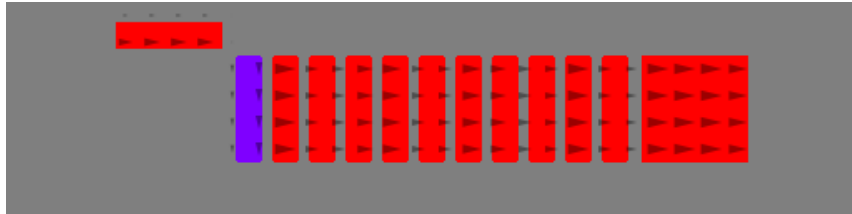


Figure 2.7: After removing the clocking field, the input magnet starts the flipping process by rendering the first chain magnet in the '0' state, i.e., magnetized downwards.

The demagnetizing field of the first magnet is then altered so that it is able to switch the magnetization of the next magnet in the chain to the other stable state, and so on. In this manner the input magnet induces logic propagation. A stabilizing magnet can be placed at the end of the chain to prevent back-propagation and stabilize the chain [25]. Figure 2.8 shows the end state of the system after the clocking field has been turned off and successful signal propagation is completed.

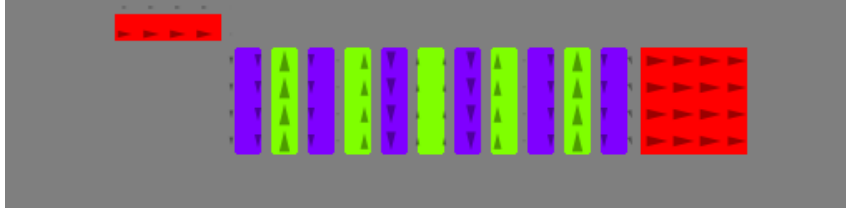


Figure 2.8: After successful logic propagation, the NML chain displays antiferromagnetic ordering.

NML offers benefits which makes it a contender for replacing CMOS technology. It has no stand-by power consumption; information, i.e., the magnetization state, is stored after the computation is carried out. Compared to CMOS technology NML allows for greater integration density and NML devices are also able to dissipate less energy in the switching process than CMOS devices [26].

There are some challenges that need to be addressed before NML devices are able to replace CMOS technology. The main concern is the reliability of NML systems. Error rates are high, especially at room temperature where thermal energy induces spontaneous switching of the magnets. Misalignment of the clocking field has shown to be a source of increased error probability. NML systems are sensitive to only a few degrees misalignment of the clocking field off the easy axis. Enhancing the intermagnet coupling can reduce the effects of angular misalignment by either decreasing the intermagnet distance or increasing the thickness of the magnets [27]. The small dimensions of the magnets pose challenges in the fabrication process as magnet deformations can also influence the error rates of NML chains.

Factors that affect the reliability of NML systems are nanomagnet geometry, intermagnet spacing and magnet material. Several studies have investigated shape engineering of nanomagnets in order to enhance hard axis stability [28]. Examples are the introduction of slanted edges [29] and concave nanomagnets [30, 31]. Magnets with higher aspect ratios have shown to exhibit lower error rates in signal propagation than magnets of lower aspect ratio [32]. Decreasing the intermagnet spacing enhances the coupling between adjacent magnets and leads to greater success rate of signal propagation [6, 8]. Shah *et al.* demonstrated an error rate improvement of 46 % when reducing the intermagnet spacing from 30 nm to 10 nm [32].

Most materials that have been investigated for use in NML exhibit uniaxial anisotropy; the

easy axis lies along the long dimension of the magnet. However, having two magnetocrystalline easy axes, along both width and height of the magnet, would enhance the hard axis stability of the magnets. This can be obtained by choosing a material exhibiting biaxial anisotropy [8, 30]. For permalloy Gu *et al.* showed that error free signal propagation is possible for a chain consisting of 24 magnets when biaxial anisotropy was incorporated in the system [8]. To further stabilize the magnetization states along the shape anisotropy hard axis one can introduce another anisotropy term in addition to the biaxial anisotropy. An experimental approach is to couple the NML system to a material exhibiting uniaxial anisotropy along the shape anisotropy hard axis [33].

As the clocking field is the dominant energy in NML devices, alternatives to the clocking field have been explored [34]. Examples are utilizing the spin-Hall effect [35] and using straintonic multiferroic logic, a version of NML, and shaping the voltage pulse which controls switching of the nanomagnets [36]. The latter NML system has also shown reduced error rates compared to traditional NML.

Chapter 3

Model System and Simulation Procedures

This chapter deals with practical aspects of the simulations and material specific properties. Section 3.1 describes LSMO, the material used in the simulations. The simulation software, MuMax3, is presented in section 3.2. Section 3.3 gives an overview of the material parameters used. The chapter is concluded by describing the simulation procedures in section 3.4.

3.1 Model system

The material studied is the complex oxide $\text{La}_{0.7}\text{Sr}_{0.3}\text{MnO}_3$, abbreviated LSMO. The perovskite material has a pseudocubic crystal structure, which can be seen in figure 3.1. Lanthanum (La) and strontium (Sr) atoms are situated on the corners of the cube. 70 % of the corner atoms are La and the remaining 30 % are Sr. Each face of the cube has an oxygen (O) atom in the center, forming an oxygen octahedron. A manganese (Mn) atom is situated in the cube center.

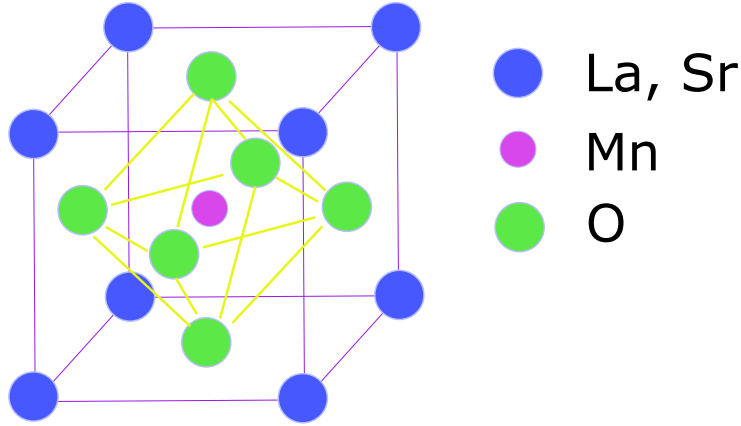


Figure 3.1: An LSMO unit cell showing the pseudocubic perovskite crystal structure.

The Curie temperature of LSMO lies between 320 K and 370 K [12]. It is a single crystalline material exhibiting biaxial crystal anisotropy. The preferred magnetization axes, the easy axes, are along the $\langle 110 \rangle$ crystallographic directions. The hard axes are along the $\langle 100 \rangle$ directions [37]. The x-axis in the model system is chosen to coincide with the $[110]$ -direction, making the x- and y-axes parallel with the LSMO easy axes. An illustration can be seen in figure 3.2.

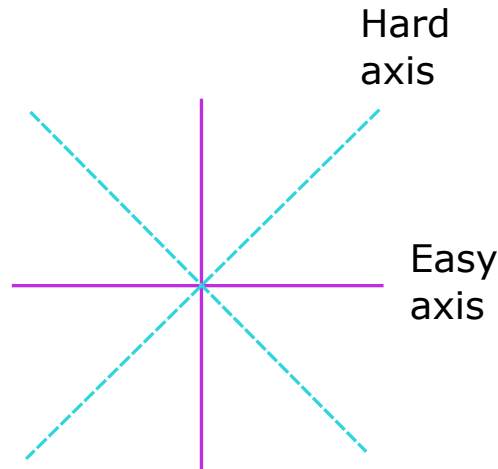


Figure 3.2: Sketch of the easy and hard axes of the model system, with the easy axes aligning with the coordinate axes.

Fabrication of LSMO is being carried out by the oxide electronics group at NTNU using pulsed laser deposition. Thin films of (001)-oriented LSMO have been modelled with thicknesses ranging from 10 nm to 50 nm.

3.2 MuMax3

The GPU-accelerated software MuMax3 [15] has been used to perform the micromagnetic simulations. MuMax3 is an open-source program which is specialized for micromagnetic simulations. In the past most micromagnetics software performed the simulations on the CPU. An example is OOMMF, which is a widely used program. Running the simulations on the GPU allows for running many small tasks in parallel, which is suitable for numerically solving differential equations like the Landau-Lifshitz equation (2.2).

The material is made up of stacked orthorhombic cells, of user-defined cell dimensions. The magnetization is assumed to be uniform within each cell. For this assumption to be valid, the requirement $l_{cell} < l_{ex}$ must be upheld; the cell dimensions cannot exceed the exchange length. As long as the cell size is smaller than the exchange length, the spins in the cell will align in a close to parallel configuration, making it a reasonable assumption to model the magnetization as uniform throughout the cell.

For calculating the reduced magnetization, MuMax3 utilizes the following version of the Landau-Lifshitz equation (2.2):

$$\tau_{LL} = \frac{\gamma_{LL}}{1 + \alpha^2} (\vec{m} \times \vec{B}_{eff} + \alpha (\vec{m} \times (\vec{m} \times \vec{B}_{eff}))), \quad (3.1)$$

where γ_{LL} is the gyromagnetic ratio, α a dimensionless damping parameter and \vec{B}_{eff} is the effective magnetic flux density [15].

The reduced magnetization, \vec{m} , of each simulation cell is stored in three components; one for each spatial dimension:

$$\vec{m} = [m_x, m_y, m_z]. \quad (3.2)$$

\vec{m} is related to the total magnetization by equation 2.4. The finite-difference method is utilized in order to calculate the magnetization of the material.

The average value of the reduced magnetization is found by calculating the norm of the averaged spatial components:

$$m = \sqrt{\langle m_x \rangle^2 + \langle m_y \rangle^2 + \langle m_z \rangle^2}. \quad (3.3)$$

For simplicity, m is from now on referred to as the magnetization.

Figure 3.3 demonstrates how MuMax3 uses colors and triangles to display the magnetization directions in the material.

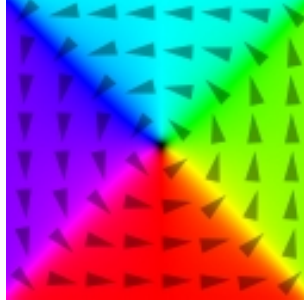


Figure 3.3: Illustration of the magnetization directions in a 256 nm x 256 nm magnet, and the color scheme used in MuMax3.

In order to calculate the energy contributions to the effective magnetic field in equation 2.3, some parameters describing the material under investigation are needed:

- The anisotropy constant which indicates the strength of the magnetocrystalline anisotropy. For uniaxial anisotropy, the constant is K_u , and in the case of biaxial anisotropy, K_{c1} is the cubic anisotropy constant.
- The exchange stiffness, A_{ex} , the value of which depends on how strongly the electron spins interact. The exchange energy is linearly dependent on the exchange stiffness [38]. For $A_{ex} > 0$, the electrons prefer a parallel spin alignment, and a negative value favors antiparallel spins.
- The saturation magnetization, M_s . As discussed in section 2.1, it is the maximum magnetization value which is obtained when a magnetic field is applied and all of the domains align with the magnetic field direction.
- The dimensionless damping parameter, α , which describes the magnetization's precession around the magnetic field direction.

Assigning cells to material groups called regions allows for having a wide range of material parameters in different parts of the material. An illustration is given in figure 3.4, where one material is assigned to region 1, and the second material to region 2. If cells are not specifically assigned to a region, they fall into region 0 by default.

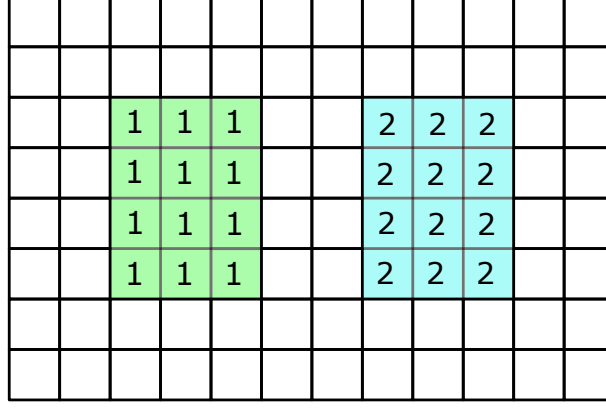


Figure 3.4: The cells of two materials can be assigned to different regions (1 and 2) in order to differentiate the material parameters.

3.3 Material parameters

Figure 3.5 shows the saturation magnetization, M_s , for a typical LSMO thin film made by the oxide electronics group at NTNU. The curve is based on measurements of the saturation magnetization for temperatures ranging from 50 K to 400 K, measured by a Versalab vibrating sample magnetometer. The measurement sample was a 112 unit cell thick film of LSMO grown on a (001)-oriented SrTiO_3 substrate.

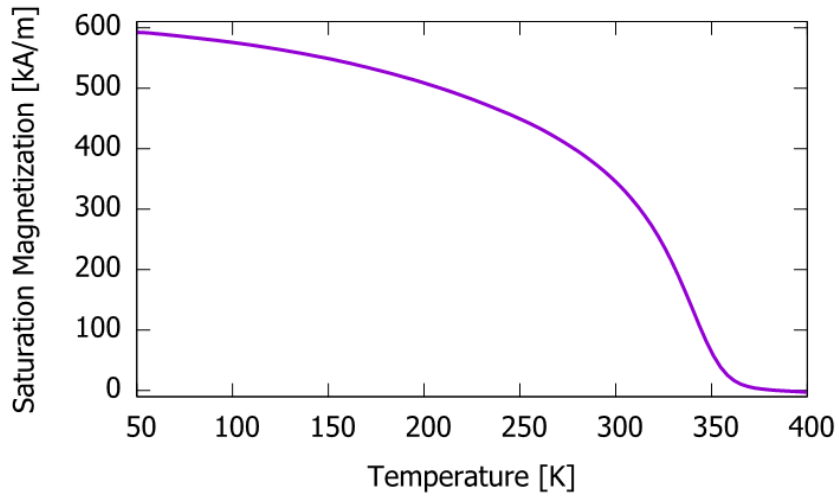


Figure 3.5: Plot displaying the saturation magnetization as a function of temperature for an LSMO thin film made by the oxide electronics group.

Another temperature dependent material parameter is the cubic anisotropy constant, K_{c1} . The values used in this work are based on work by Lee *et al.* [39], see figure 3.6. The anisotropy constant is found for temperatures between 32 and 230 K. The green line in figure 3.6 results from the assumption that K_{c1} is uniform throughout a patterned micromagnet. The blue line in figure 3.6 accounts for edge effects and treats the anisotropy constant as uniform in the center of the sample, and decaying toward the edges. The values corresponding to the blue line have been used in this work.

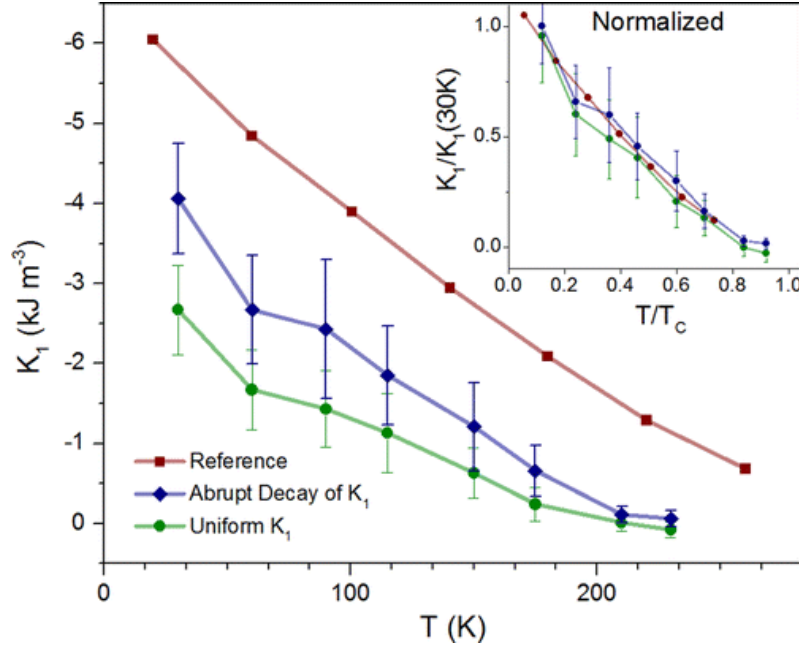


Figure 3.6: Plot of the magnetocrystalline anisotropy constant vs. temperature. Reprinted with permission from Lee *et al.* [39]. Copyright 2016 American Chemical Society.

As figures 3.5 and 3.6 show, both the saturation magnetization and the cubic anisotropy constant decrease with increasing temperature. Table 3.1 gives values for M_s and K_{c1} for temperatures 50 K, 100 K and 300 K.

Table 3.1: An overview of the temperature dependent material parameters and their values at 50 K, 100 K and 300 K.

Material parameter	Symbol	Unit	50 K	100 K	300 K
Saturation magnetization	M_s	kA/m	590	570	350
Cubic anisotropy constant	K_{c1}	J/m ³	3000	2100	100

The exchange stiffness, A_{ex} , was initially set to 1.7×10^{-12} J/m, based on work by Takamura *et al.* [13]. The magnetic exchange length, l_{ex} , can be found using equation 2.5. A consequence of the saturation magnetization's dependence on temperature is that the exchange length increases with temperature. For 50 K, l_{ex} has a value of approximately 2.8 nm. Therefore, a cell size of 2.0 nm is a safe choice for temperatures of 50 K and above.

Using small simulation cells results in longer simulation time. Therefore, when simulating systems consisting of several magnets, larger cells would be beneficial. In the following, a somewhat larger simulation cell is chosen in order to reduce simulation time. The justification for breaking the requirement $l_{cell} < l_{ex}$, is that the nanomagnets used when simulating chains have been verified to be monodomain, both in experiments performed in the oxide electronics group as well as in the specialization project preceding this thesis work.

The specialization project focused on monodomain formation in single magnets of LSMO [40]. One of the results from this specialization work is shown in figure 3.7. The heat map shows which magnets become monodomain after initializing the system with uniform magnetization in the +x-direction and letting the system relax. The magnets were rectangles with rounded corners, simulated at 100 K. The thickness was 15 nm. For each combination of width (along the x-axis) and height (y-axis), 100 simulations were run. The color of each point in the heat map indicates how many of the 100 simulations resulted in monodomain states.

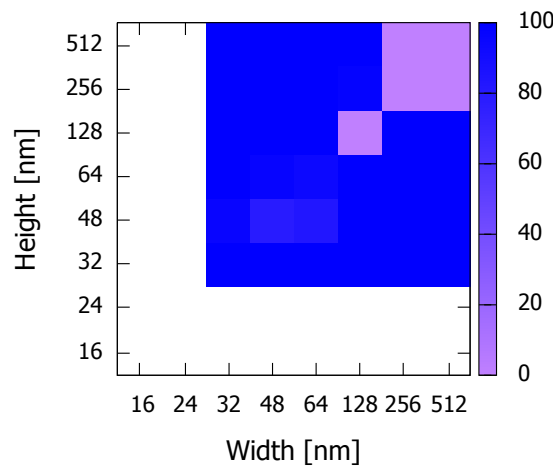


Figure 3.7: A result from the specialization project. For a given width and height, the heat map indicates how many of the 100 simulation resulted in monodomain states.

The cell size was increased to 8.0 nm, and in accordance with equation 2.5 the exchange stiffness was adjusted to 1.4×10^{-11} J/m. The reason for not making the cells even larger is the magnet geometry. When making rectangles with "rounded" corners, the corner cells are removed from the initial rectangular shape. If the cell dimensions are too large, removing one cell from each corner could potentially reduce the width of the magnet severely.

Based on the work of Luo *et al.* the damping parameter, α , was set to 1.57×10^{-3} [41]. As the model system is a thin film, it is common practice to only use one cell in z-direction. The consequence is that there will be no domain formation in this direction since the magnetization is uniform within each cell. The cell thickness (in z-direction) was varied from 10 nm to 50 nm.

3.4 Simulation procedures

Scripts used for the simulations can be found in appendix A; nanomagnet chains in A.1 and fanout structure in A.2.

3.4.1 Nanomagnet chains

In this work a system of 24 magnets was chosen as our model system for a nanomagnetic chain, see figure 3.8. The leftmost magnet is called the start magnet as it initiates a chain reaction in the 22 successive identical magnets. The rightmost magnet is the stop magnet which has a stabilizing effect on the chain. The width of the stop magnet is twice the height of the chain magnets.



Figure 3.8: An image showing the system setup of the nanomagnet chain. To the left is a single start magnet, followed by a chain of 22 identical magnet, and the last magnet is a stabilizing stop magnet.

The systems were initialized with a uniform magnetization in the +x-direction. Initially

a magnetic field was applied in the same direction to prohibit the signal propagation to start. The magnetic field strength was reduced in steps of 1 mT until the signal had propagated across the chain and the system had stabilized. The simulation was run for 1 ns after each reduction in the magnetic field.

In order to reduce simulation time, some effort was used to determine adequate values for the initial magnetic field, which depend on the system parameters. The value for a given set of parameters (nanomagnet dimensions, thickness, intermagnet spacing and uniaxial anisotropy) was determined by observing the switching process of the system as the magnetic field strength was reduced in steps. An initial magnetic field of 250 mT was applied, which in all cases was large enough to induce hard axis stabilization. The magnetic field was then reduced by 1 mT and the simulation was run for 1 ns. The procedure was repeated until the magnetic field strength equaled zero. By evaluating the value of m_x , the x-component of the magnetization, an appropriate initial magnetic field strength was found.

Four variables were tested; aspect ratio, thickness, intermagnet spacing and uniaxial anisotropy. Table 3.2 gives an overview of the parameter values. A star (*) indicates the variable which is being tested. All simulations were run with parameters corresponding to a temperature of 100 K.

Table 3.2: An overview of the system variables. Each row has a star (*) which indicates the variable being tested.

Variable	Symbol	AR	t	d	K_u
Aspect ratio	AR	*	15	32	0
Thickness	t	3.0	*	32	0
Intermagnet spacing	d	3.0	10, 25	*	0
Uniaxial anisotropy	K_u	3.0	10	8, 16, 32, 48	*

Nanomagnet dimensions

The specialization project formed the starting point for the choice of nanomagnet dimensions. The initial choice for nanomagnet dimensions was 128 nm \times 512 nm, which according to figure 3.7, one of the results from the specialization project, should result in

monodomain states. The reason for choosing relatively large magnets was keeping the dimensions so large that experimental verification was possible. However, the methodology is directly transferable to systems of smaller magnets.

10 simulations were run for the $128 \text{ nm} \times 512 \text{ nm}$ magnets. Next, smaller magnets with $64 \text{ nm} \times 256 \text{ nm}$ dimensions were simulated following the same procedure. Aspect ratios ranging from 1.5 to 4.0 were tested. The width of the magnets was kept constant at 64 nm. Six values for the height were used: 96 nm, 128 nm, 160 nm, 192 nm, 224 nm and 256 nm. The magnet thickness was 15 nm and the intermagnet spacing was 32 nm. 100 simulations were run for each parameter set.

Thickness

The next parameter to be varied was the thickness of the magnets. Changing the thickness of the magnets influences the dipolar coupling between adjacent nanomagnets. Increasing the thickness (and volume) of the chain magnets leads to an increase in the strength of the demagnetizing field, which results in stronger coupling between the nanomagnets.

The magnet dimensions were $64 \text{ nm} \times 192 \text{ nm}$. 100 simulations were run for each of the thicknesses 10 nm, 15 nm, 20 nm, 25 nm, 30 nm and 50 nm. The intermagnet spacing was $d = 32 \text{ nm}$ for all thicknesses.

Energy landscape In order to keep the chain magnets stable with a magnetization along the shape anisotropy hard axis until the signal reaches the magnets and induces a flipping of the magnetization, hard axis stabilization is necessary. The chain configuration has a stabilizing effect on the magnets. Enhancing the hard axis stability further can lead to a dip in the energy landscape for magnetization in the +x-direction. Carlton *et al.* obtained a local energy minimum, or hard axis metastability, for Co nanomagnets by introducing biaxial anisotropy [25].

An energy landscape is presented by displaying the energy of a single magnet inserted in a chain as a function of the magnetization angle, θ . Figure 3.9 shows the magnetization states for $\theta = -90^\circ, -45^\circ, 0^\circ, 45^\circ$ and 90° . $\theta = 0^\circ$ represents magnetization along the shape anisotropy hard axis, i.e., in the +x-direction.

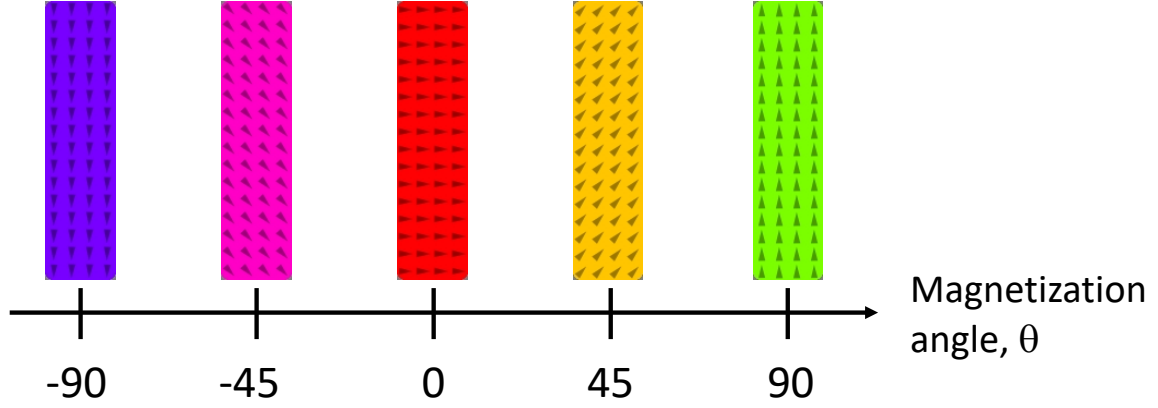


Figure 3.9: An illustration of the magnetization states of a single magnet for magnetization angles $\theta = -90^\circ$, -45° , 0° , 45° and 90° .

The test magnet was inserted in a chain of identical magnets, illustrated in figure 3.10. Surrounding the test magnet are magnets which are all initialized with a magnetization in the +x-direction, i.e., with a magnetization angle of $\theta = 0^\circ$. The test magnet in the figure is magnetized in the +y-direction, with $\theta = 90^\circ$.

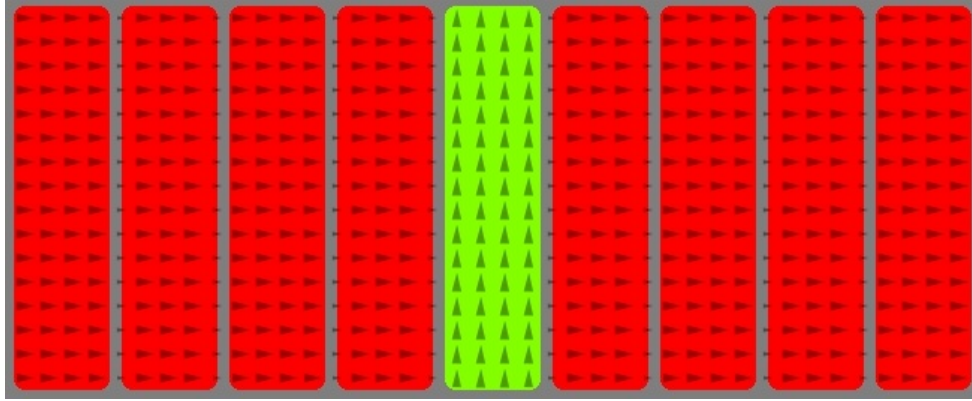


Figure 3.10: A nanomagnet chain with the test magnet in the middle. All of the surrounding magnets are magnetized in the +x-direction.

Intermagnet spacing

Two thicknesses were chosen for investigation; $t = 10$ nm and $t = 25$ nm. The reason for choosing these thicknesses was to figure out if decreasing the spacing would lead to higher success rates. Values for the intermagnet spacing were $d = 8$ nm, 16 nm, 32 nm and 48 nm.

Energy landscapes were made, using six values for the intermagnet spacing; $d = 1$ nm, 2 nm, 4 nm, 8 nm, 16 nm and 32 nm. For $d < 8$ nm, the cell size was adjusted to 1 nm. For these simulations, the value for the exchange stiffness was set to 1.7×10^{-12} J/m.

Uniaxial anisotropy

In the specialization project, it was shown that a local energy minimum can be obtained for magnetization along the shape anisotropy hard axis when adding uniaxial anisotropy to an LSMO magnet [40]. Figure 3.11 shows the energy landscape for the magnet, for four values of the uniaxial anisotropy. In practice, a uniaxial anisotropy term can be incorporated in the system by coupling the LSMO chains to an antiferromagnet, for example LaFeO_3 [42] or SrTiO_3 [33].

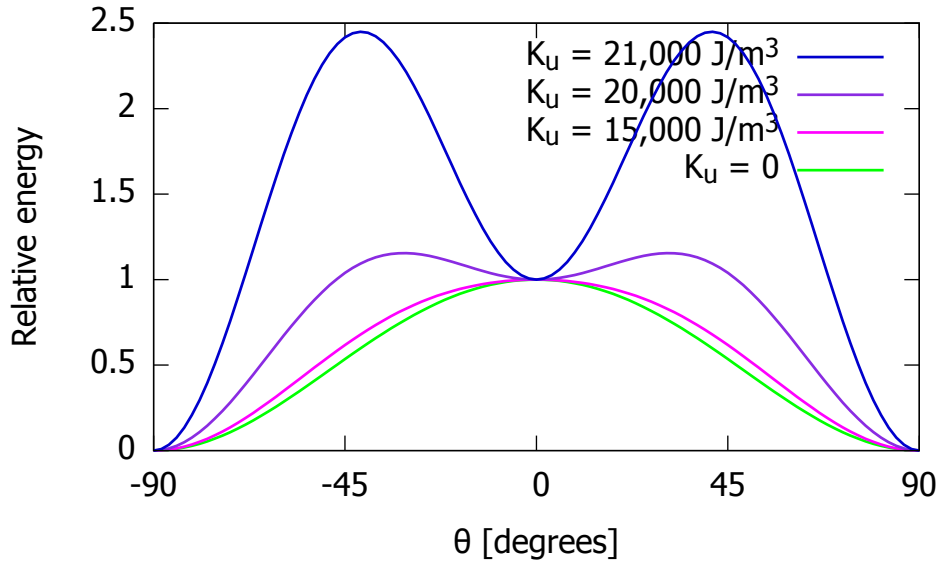


Figure 3.11: The energy landscape of a single LSMO magnet shows that hard axis metastability was obtained when adding a uniaxial anisotropy along the shape anisotropy hard axis.

Uniaxial anisotropy was included in the +x-direction, along the shape anisotropy hard axis. Systems of varying magnet thickness and intermagnet spacing were studied. The thicknesses were 10 nm, 15 nm, 20 nm, 25 nm and 50 nm. The spacings were 8 nm, 16 nm, 32 nm and 48 nm. Starting from $K_u = 0$, the strength of the uniaxial anisotropy was increased with 2 kJ/m^3 for each parameter set until the system was too stable to allow

for logic propagation. For each combination of thickness, spacing and uniaxial anisotropy 10 simulations were run.

3.4.2 Nanomagnet fanout structure

The first step towards making logic gates was controlling signal propagation in a horizontal chain of magnets. In order to build complex NML systems, we must be able to transfer signals from horizontal chains to vertical chains. Therefore, a fanout structure was studied, consisting of three horizontal chains and a vertical chain.

Figure 3.12 shows the setup of the branched structure. Initially, the magnets were magnetized in the $+x$ -direction, along their shape anisotropy hard axis. Signal propagation starts in the same way as for the nanomagnet chains; the chain reaction is initiated due to the demagnetizing field of the start magnet, in the bottom left of the figure. The signal then propagates to the middle of the bottom chain where it splits up. The signal which propagates upwards again splits at the middle of the vertical chain.

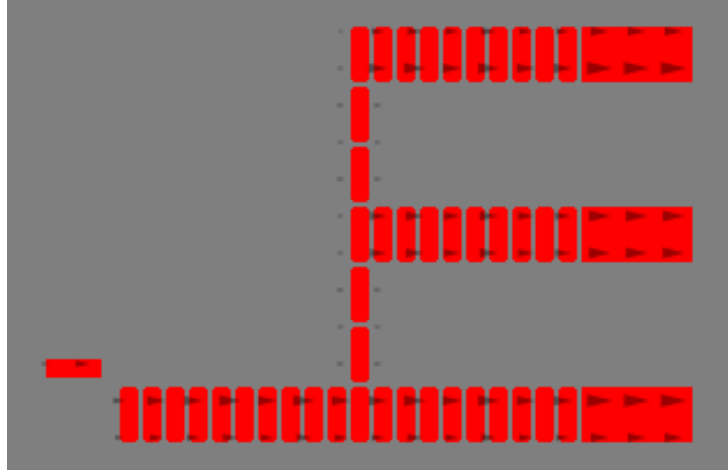


Figure 3.12: A figure showing the setup for the fanout structure that was studied, here initialized with hard axis magnetization in the $+x$ -direction.

There are some requirements for a successful signal propagation in this system. Firstly, every magnet must stay magnetized along the hard axis until the signal induces a flipping of the magnetization, to either upwards or downwards magnetization. Secondly, the magnets in the horizontal chains must end up with an antiferromagnetic ordering, and for the vertical chains there must be a ferromagnetic alignment.

When starting to experiment with the fanout structure, the system parameters chosen were "safe", i.e., parameters which gave a 100 % success rate when looking at nanomagnet chains. The chain magnets were of dimensions $64 \text{ nm} \times 192 \text{ nm}$, thickness 50 nm , intermagnet spacing 16 nm and uniaxial anisotropy $K_u = 18 \text{ kJ/m}^3$.

Two methods were used for applying the magnetic field. The main method used was the same as for the nanomagnet chains, i.e., reducing the strength of the magnetic field by 1 mT , running the simulation, and then repeating the procedure until the system had stabilized. The other approach was to abruptly remove the magnetic field.

The system was expanded with additional magnets whose function was to try to stabilize the magnets of the vertical chain, seen in figure 3.13. The initial geometry of the additional magnets was squares with sides which were a factor 1.8 larger than the width of the chain magnets, i.e., 115.2 nm .

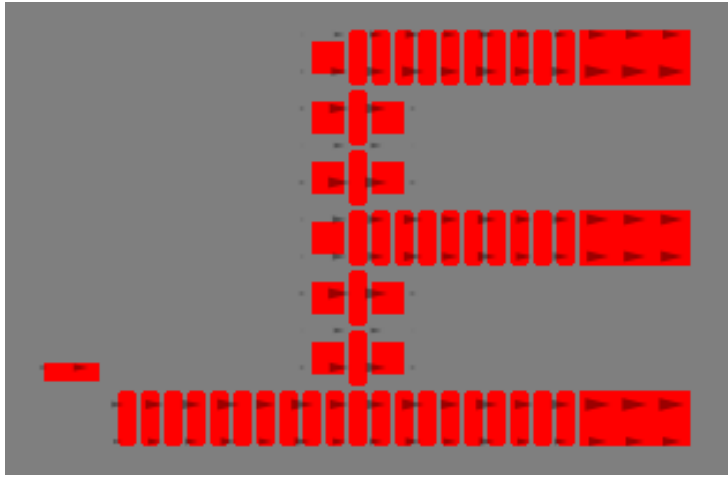


Figure 3.13: A modified fanout structure including stabilizing magnets in close proximity to the vertical magnets. The stabilizing magnets are squares with sides of 115.2 nm .

The last part of the simulations included varying the dimensions of the stabilizer magnets along the vertical chain in combination with testing the vertical intermagnet spacing. The height of the stabilizer magnets was varied between 115.2 nm and 192 nm , while the width ranged between 115.2 nm and 384 nm , i.e., not only square stabilizer magnets were tested. The vertical intermagnet spacing ranged from 16 nm to 48 nm .

Chapter 4

Results and Discussion

The main focus in this work has been on studying nanomagnet chains. Section 4.1 presents results for chains with varying system parameters; aspect ratio of the magnets in section 4.1.1, thickness in section 4.1.2, intermagnet spacing in section 4.1.3 and finally uniaxial anisotropy in section 4.1.4. Section 4.2 explores a more complex NML structure, the fanout structure.

4.1 Nanomagnet chains

When studying chains of nanomagnets, the success rate of signal propagation is used as a measure to compare different systems. Successful propagation is defined as the process in which the demagnetizing field of the start magnet (see figure 3.8) induces a chain reaction resulting in antiferromagnetic ordering of the magnets in the chain.

A magnetic field was applied in the +x-direction in order to initialize the chain magnets along their shape anisotropy hard axis. Values for the initial magnetic field were found by investigating the value of m_x as the field was ramped down in steps. The system was generally stable for values between $m_x = 0.998$ and $m_x = 0.997$. When the magnetic field strength was low enough for the system to initiate the switching process, the magnetization value started to decline. When the signal propagation started, the magnetization value was below 0.996. The initial magnetic field for a given parameter set was set to the value corresponding to the step before m_x was reduced to under 0.997.

4.1.1 Nanomagnet dimensions

For the $128 \text{ nm} \times 512 \text{ nm}$ magnet chains, 10 simulations were run. Figure 4.1 shows one of the results. Magnet number 15 in the chain displays an unexpected final state. The magnet consists of three domains. According to the heat map of figure 3.7, the magnets should relax into monodomain states. Apparently, monodomain states are not always the final state when the magnets are inserted in a chain.

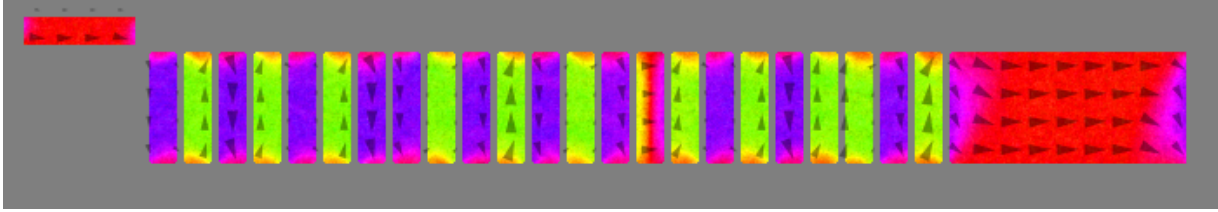


Figure 4.1: A final state of a chain of $128 \text{ nm} \times 512 \text{ nm}$ magnets where magnet number 15 consists of three domains.

Reducing the magnet size to $64 \text{ nm} \times 256 \text{ nm}$ eliminated the issue of domain formation in the chain magnets. The simulations resulted in one of two scenarios, shown in figure 4.2; successful propagation of the signal (figure 4.2a) or unsuccessful propagation (figure 4.2b).

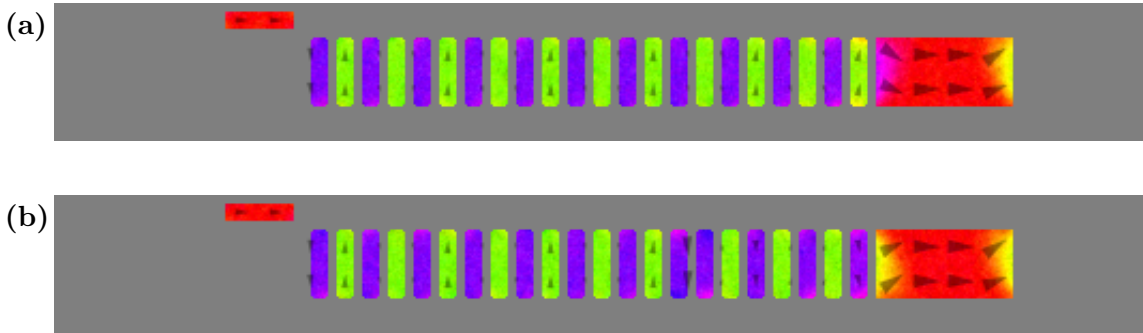


Figure 4.2: Signal propagation for the chains made up of $64 \text{ nm} \times 256 \text{ nm}$ magnets resulted in either (a) successful or (b) unsuccessful propagation.

After confirming that magnets of dimensions $64 \text{ nm} \times 256 \text{ nm}$ remained monodomain after propagation, aspect ratio tests were conducted. The magnet width was held constant at 64 nm , and the height was varied from 96 nm to 256 nm in steps of 32 nm . The results are shown in figure 4.3. The success rates were in the range from 76% to 81% . The highest

success rate was found for magnets of aspect ratios 3.0 and 3.5, of which both simulation sets resulted in a success rate of 81 %.

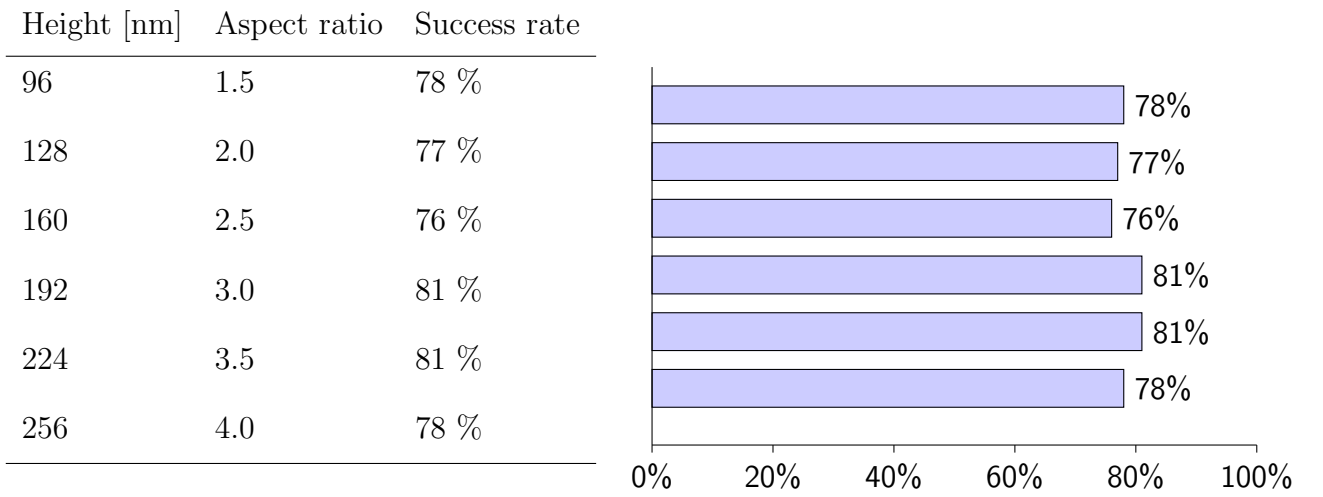


Figure 4.3: Figure showing the success rates of the chains with 64 nm wide magnets.

In literature, there are not many simulation studies on success rate dependence on aspect ratio for NML chains of materials exhibiting biaxial magnetocrystalline anisotropy. For supermalloy, a material with uniaxial anisotropy, Shah *et al.* reported higher success rates for magnets of aspect ratio 2.0 ($120 \times 60 \times 20 \text{ nm}^3$) than for magnets of an aspect ratio of 1.5 ($120 \times 90 \times 20 \text{ nm}^3$) [32]. Yang *et al.* recommended using an aspect ratio between approximately 1.4 and 1.7 for a chain of supermalloy magnets [11]. However, due to LSMO's biaxial magnetocrystalline anisotropy, the magnets are more stable along the shape anisotropy hard axis, making it possible to utilize magnets of higher aspect ratio.

Based on the results in figure 4.3, where the success rate is highest for aspect ratios 3.0 and 3.5, it seems as the ideal aspect ratio for the LSMO system is higher than for materials exhibiting uniaxial anisotropy. As it is beneficial for devices to have smaller components, it was chosen to proceed with the smaller magnets, i.e., of dimensions $64 \text{ nm} \times 192 \text{ nm}$. Another benefit of choosing the magnets of lower aspect ratio is that the system requires a lower clocking field [9].

4.1.2 Thickness

The success rates resulting from varying the magnet thickness are shown in figure 4.4. From a success rate of 50 % for the thinnest magnets of $t = 10$ nm, the success rate increases rapidly to 81 % for a 15 nm thin film and almost doubling (96 %) for 20 nm thick magnets. For $t > 25$ nm, all of the simulations resulted in successful propagation.

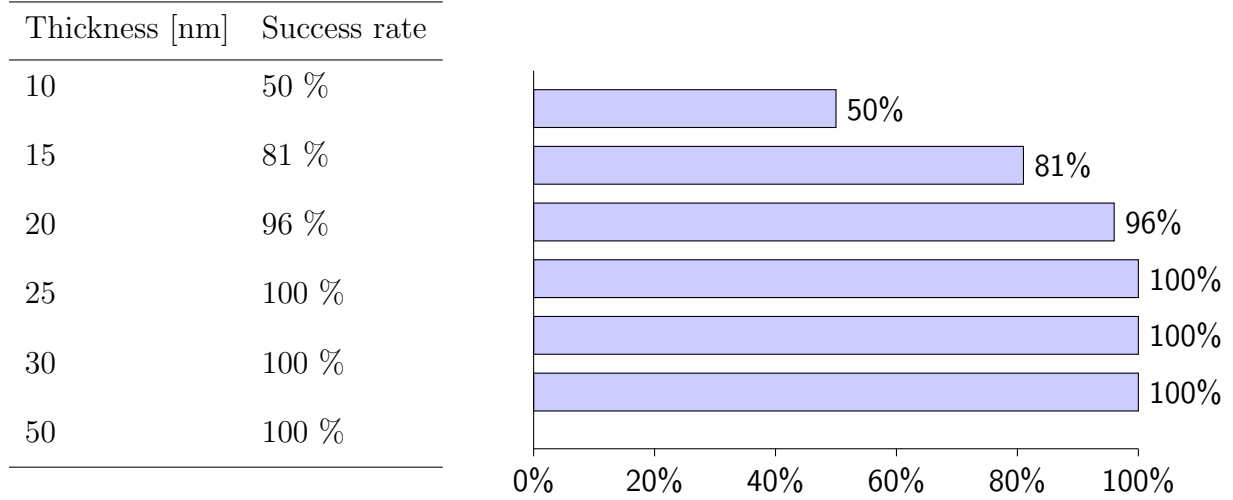


Figure 4.4: Figure displaying the success rates for varying thickness of the $64 \text{ nm} \times 192 \text{ nm}$ magnets.

The success rates increase as the thickness (and volume) of the magnets increase. As the magnets increase their volume, the dipolar coupling between the magnets in the chain increases, enhancing the chain's stabilizing effect. It could be tempting to use the thicker magnets which give a 100 % success rate. However, using thin magnets are beneficial because fabrication is less demanding for thinner films. In addition, a weaker coupling between the magnets requires a lower magnetic field when resetting the clocking field.

Energy landscapes for thicknesses ranging from 10 nm to 50 nm are shown in figure 4.5. Qualitatively, the graphs are similar. The energy is maximized when the magnetization direction of the test magnet is $\theta = \pm 180^\circ$, i.e., opposing the chain magnets which are all magnetized in the $+x$ -direction, with $\theta = 0^\circ$. There are two global energy minima. The magnetization angle where the energy minima occur is dependent on the magnet thickness. The energy minima moves further away from $\pm 90^\circ$ and closer to 0° as the

thickness increases, i.e., as a result of a stronger coupling between the magnets.

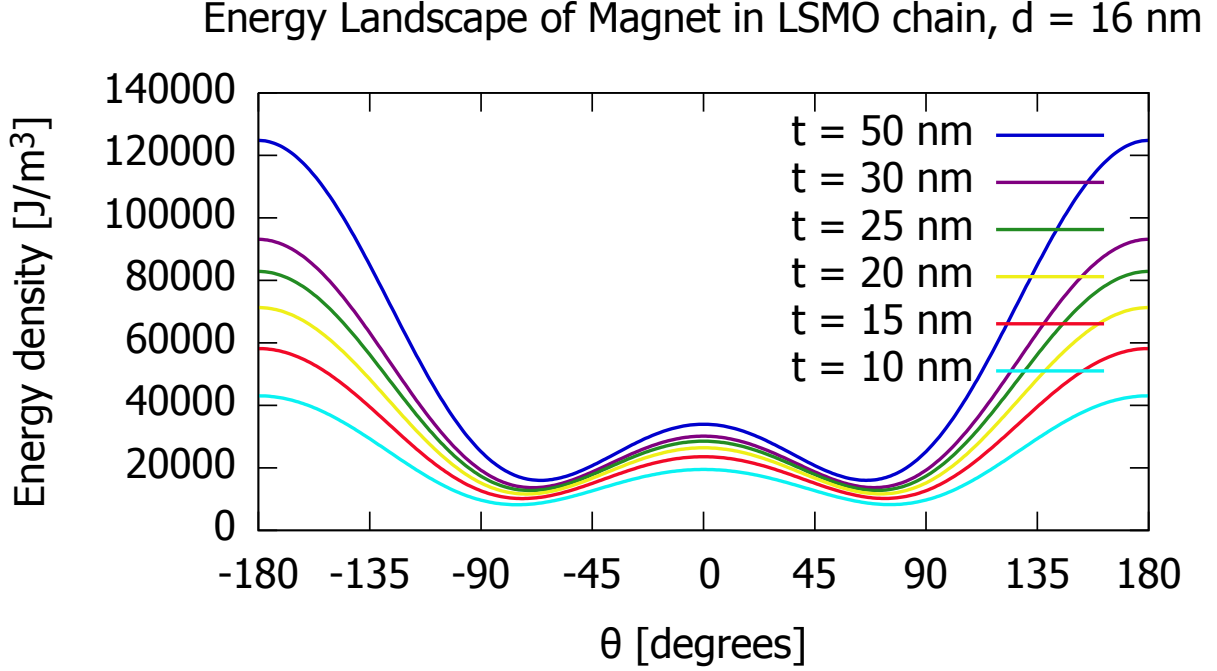


Figure 4.5: Figure showing energy landscapes for thicknesses ranging from 10 nm to 50 nm.

The energy difference between the maximum and the minimum energy is a measure for the strength of the coupling between the adjacent magnets. The largest energy difference is seen for the $t = 50$ nm magnets, with the difference decreasing as the thickness decreases. Ideally, one would have a local energy minimum at $\theta = 0^\circ$, leading to an enhancement in the hard axis stabilization. However, hard axis metastability is not seen for these magnets.

4.1.3 Intermagnet spacing

Figures 4.6 and 4.7 give the success rates for varying intermagnet spacing, for thicknesses $t = 10$ nm and $t = 25$ nm, respectively.

Intermagnet spacing [nm]	Success rate
8	94 %
16	69 %
32	50 %
48	27 %

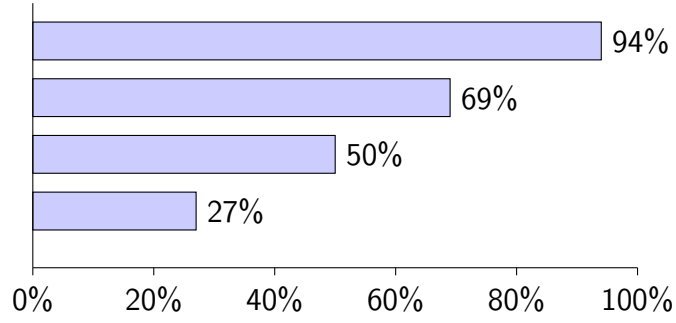


Figure 4.6: Success rate dependence of intermagnet spacing for 10 nm thick magnets

For $t = 10$ nm, the effect of increasing the magnets' dipolar coupling by bringing them closer together is evident. From only half of the chains resulting in successful propagation at $d = 32$ nm, 94 out of 100 simulations were successful for an intermagnet spacing of 8 nm.

Intermagnet spacing [nm]	Success rate
8	100 %
16	100 %
32	100 %
48	90 %

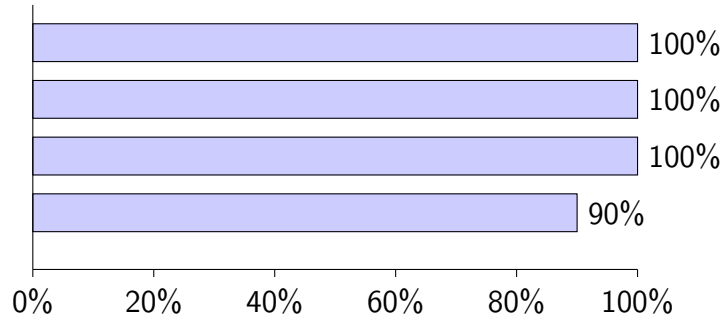


Figure 4.7: Success rate dependence of intermagnet spacing for 25 nm thick magnets

As discussed in the previous section, increasing the magnet thickness results in more stable magnets. The effect can be seen by comparing the tables for $t = 10$ nm and $t = 25$ nm. For spacing $d = 32$ nm, the success rate is twice as high for the thicker magnets. Where a success rate of 94 % was obtained for the $t = 10$ nm magnets by having a small separation of $d = 8$ nm, the spacing can be substantially higher for the $t = 25$ nm magnets. For these magnets, a 100 % success rate was obtained for magnets with an intermagnet spacing up

to $d = 32$ nm.

When studying an NML system of 20 nm thick supermalloy magnets, Shah *et al.* observed an increase in the success rate from 24 % for $d = 30$ nm to 70 % when decreasing the intermagnet spacing to 10 nm [32]. The same trend is seen for the LSMO chains; for the 10 nm thick magnets, the success rate increases from 50 % to 94 % when reducing the intermagnet spacing from 32 nm to 8 nm.

The results are not directly comparable since the NML systems differ in the setup and in the material used. For example, the LSMO chain consists of 22 magnets whereas Shah *et al.* used a chain of 5 supermalloy magnets. However, the results seem to suggest that the LSMO system is more robust than the supermalloy system due to higher success rates for comparable variables. Even if the difference in the number of magnets in the chain is neglected and we choose parameters for comparison which work in favor of the supermalloy system, the LSMO chains seem to be the better choice for NML application. For example, comparing the LSMO system with $t = 10$ nm and $d = 32$ nm which gives a success rate of 50 % (figure 4.6), with the supermalloy system with $t = 20$ nm, $d = 30$ nm, giving a success rate of 24 %, the result is a higher success rate for the LSMO system in spite of using stricter system parameters when comparing the systems (lower thickness and higher intermagnet spacing).

Figure 4.8 shows energy landscapes for a $t = 15$ nm magnet where the intermagnet spacing varies from 1 nm to 32 nm. Similar to the energy landscape of figure 4.5, the position of the energy minima vary with the parameter which is varied, moving further away from $\pm 90^\circ$ and closer to 0° as the coupling between the magnets gets stronger. The energy maxima also occur at $\pm 180^\circ$, where the maximum value occurs for chains with the smallest intermagnet spacing ($d = 1$ nm). As these magnets experience stronger dipolar coupling than magnets with larger separation, it is more energy costly to reverse the magnetization of the test magnet. As for the energy landscape where the thickness is varied, the energy difference between the maximum and the minimum energy is a measure for how strong the coupling between the magnets is; the energy difference is greatest for $d = 1$ nm, and decreases as the intermagnet spacing is increased.

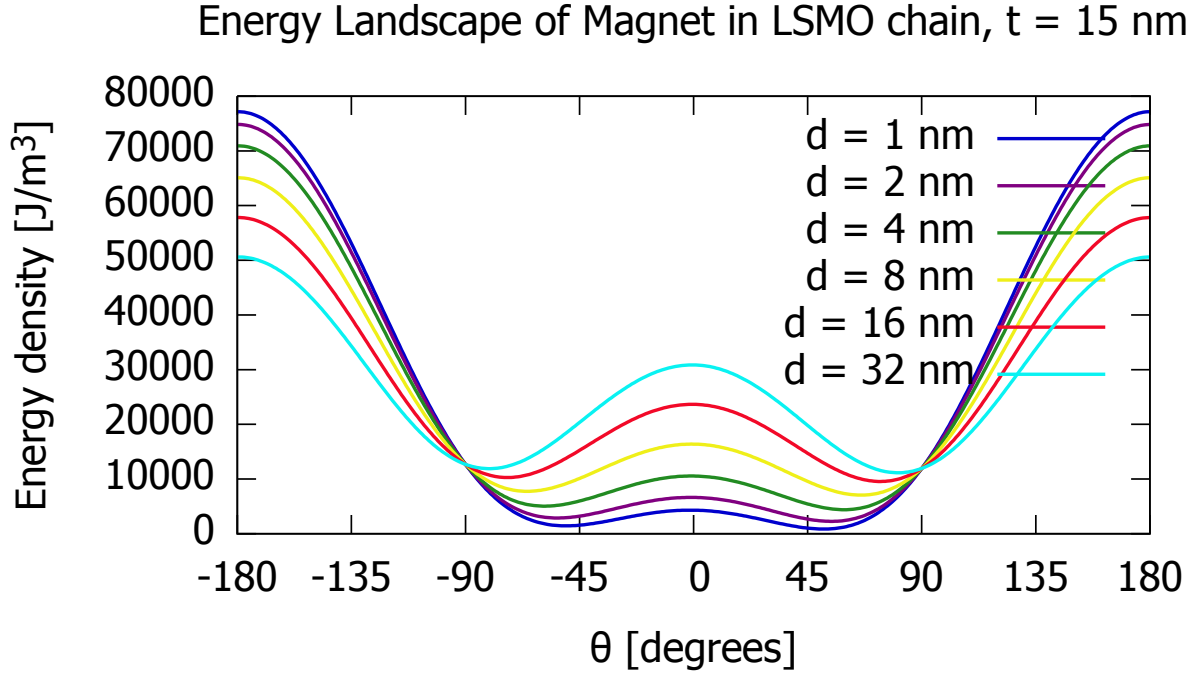


Figure 4.8: Energy landscape for various intermagnet spacing, with d ranging from 1 nm to 32 nm.

As for the energy landscape for various thicknesses, it would be desirable to have a local energy minimum at $\theta = 0^\circ$ to increase the stability of the initial magnetization state. Again, no hard axis metastability is observed for any value of the spacing. However, the energy landscape at hard axis orientation is flatter for the chains with smaller separation between the magnets, which might suggest that these systems are more stable. In terms of fabrication, the smallest values for the spacing are not currently experimentally realizable.

4.1.4 Uniaxial anisotropy

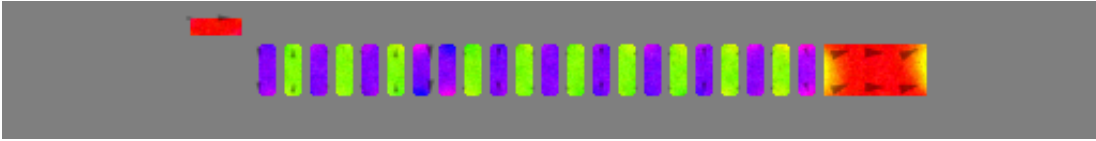
This section explores the uniaxial anisotropy and its dependence upon intermagnet spacing and thickness. Figure 4.9 shows the three groupings of the results for magnets with $t = 15$ nm and $d = 32$ nm. Successful propagation is depicted in figure 4.9a, where the magnetization states of the chain magnets align antiferromagnetically. Two types of errors occurred. One type of error was unsuccessful switching as seen in figure 4.9b, where the error occurs at magnet number 8 in the chain. Another type of error is when the uniaxial

anisotropy constant, K_u , is so high that it makes the chain too stable along the shape anisotropy hard axis, not allowing signal propagation to occur. This situation is shown in figure 4.9c, where the start magnet's demagnetizing field has altered the magnetization direction of the first chain magnet, which in turn has affected the second magnet. However, due to the hard axis stabilization, signal propagation does not occur across the chain.

(a) A successful propagation for a chain with $K_u = 0$ displays antiferromagnetic ordering.



(b) Unsuccessful signal propagation for $K_u = 0$. The error arises at magnet nr. 8.



(c) When the uniaxial anisotropy reaches a certain value, the chain's hard axis stabilization is too strong to allow for signal propagation. Here, $K_u = 24 \text{ kJ/m}^3$.



Figure 4.9: Figure showing three representative results for magnets of thickness 15 nm and intermagnet spacing 32 nm. When introducing uniaxial anisotropy to the system, the results were grouped in three categories; success, error due to unsuccessful propagation and error because of a too stable chain.

The cut-off value for the uniaxial anisotropy is defined as the minimum value of the uniaxial anisotropy which results in the situation seen in figure 4.9c, where signal propagation does no longer occur. Cut-off values for a given intermagnet spacing and thickness are given in figure 4.10.

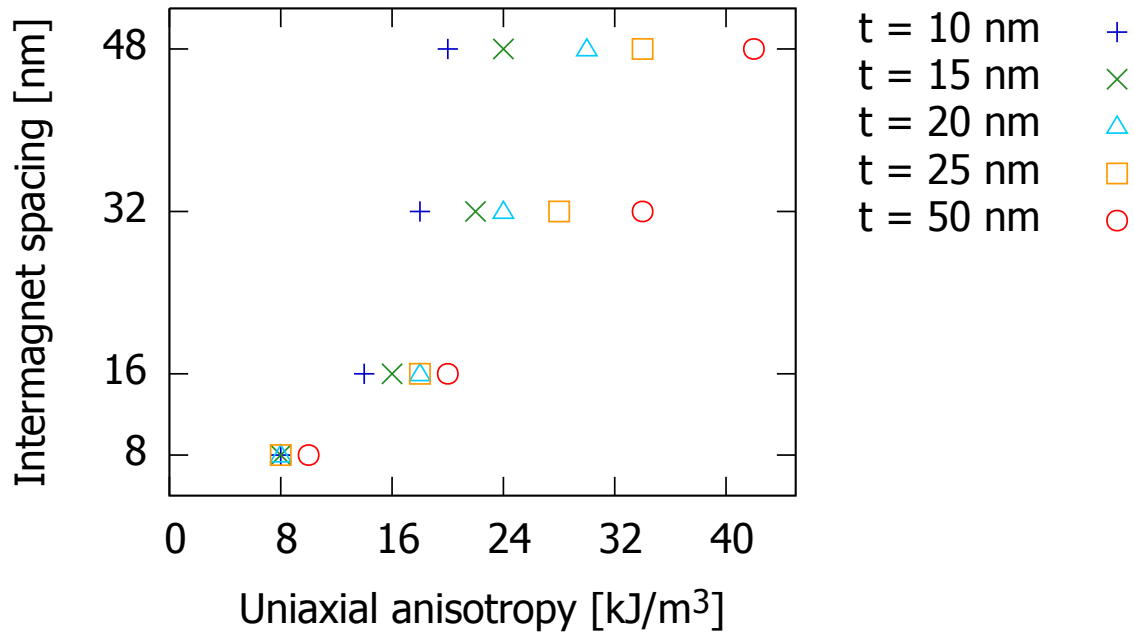


Figure 4.10: Plot showing cut-off anisotropies for when the system is too stable to allow for signal propagation.

Starting from the smallest intermagnet spacing, $d = 8$ nm, the spread in the cut-off anisotropy is small. Except for the $t = 50$ nm magnets, all of the systems have cut-off anisotropies of 8 kJ/m³. For the thickest magnets, the value is 10 kJ/m³. As the intermagnet spacing increases, the range of the cut-off anisotropies is expanded. From a spread of 2 kJ/m³ for the smallest spacing systems, the cut-off for $d = 48$ nm ranges from 20 kJ/m³ to 42 kJ/m³, a difference of 22 kJ/m³.

Larger spacing reduces the chain's stabilizing effect and more uniaxial anisotropy can be applied before reaching cut-off. The magnets of larger thickness have stronger demagnetizing fields, making the magnets more resistant to changing the magnetization direction to hard axis orientation.

Figure 4.11 shows the results for varying values of the uniaxial anisotropy and intermagnet spacing, or separation of the chain magnets. The subfigures display the results for thickness $t = 10$ nm, 15 nm, 20 nm, 25 nm and 50 nm. In the scale to the right, the green square represents 10 out of 10 successful systems. On the bottom of the scale, a red square indicates 0 successful systems. A black square means that the uniaxial anisotropy is so

strong that the chain is too stable to allow for signal propagation. Each data point belongs to a region; I, II or III. The light gray colored region I is made up of points which resulted in up to 9 successful chains. The point in which all 10 simulations were successful belong to region II. Region III, of dark gray color, is an area where the chain is too stable (due to high uniaxial anisotropy) to allow for signal propagation, i.e., it contains all black points.

Starting with the results for the 10 nm thick magnets, the lowest intermagnet spacing, $d = 8$ nm, resulted in successful propagation in 10 out of 10 cases. For $d > 8$ nm and small anisotropy values, the success rates are low. Higher success rates can be seen as K_u is increased, most evident for spacing $d = 16$ nm and $d = 32$ nm just before the chain is too stable for signal propagation.

For $t = 15$ nm, all of the simulations for $d = 8$ nm resulted in successful propagation, identical to the results for the 10 nm thick magnets. In addition, all of the simulations where the intermagnet spacing was 16 nm were successful. Compared to the figure for $t = 10$ nm, more of the simulations for $d = 32$ nm and $d = 48$ nm had successful propagation. The simulations for magnets of thickness 20 nm result in a bigger region II. Only six simulation sets resulted in error, and five of these occurred for the largest magnet separation, $d = 48$ nm.

For a thickness of 25 nm, successful propagation was the case for all systems with intermagnet spacing less than 48 nm. The result is consistent with figure 4.7, where $d = 8$ nm, 16 nm and 32 nm all resulted in a 100 % success rate for $K_u = 0$. For $d = 48$ nm, only three data points had less than 10 successful runs. Increasing the thickness to 50 nm results in an elimination of region I, i.e., all of the simulations resulted in successful chains as long as signal propagation was possible.

Region II expands as the thickness increases, which is consistent with the results from section 4.1.2 where an increase in thickness resulted in increased success rates. Considering the intermagnet spacing, it is again shown that systems of lower separation are more stable. If one would want to use magnets of 10 nm thickness, it would be safer with an intermagnet spacing of 8 nm since all of the simulations resulted in successful propagation. However, fabrication of NML chains with $d = 8$ nm is currently demanding. An alternative could be to choose a large uniaxial anisotropy, here 12 kJ/m^3 , in order use a 16 nm intermagnet spacing.

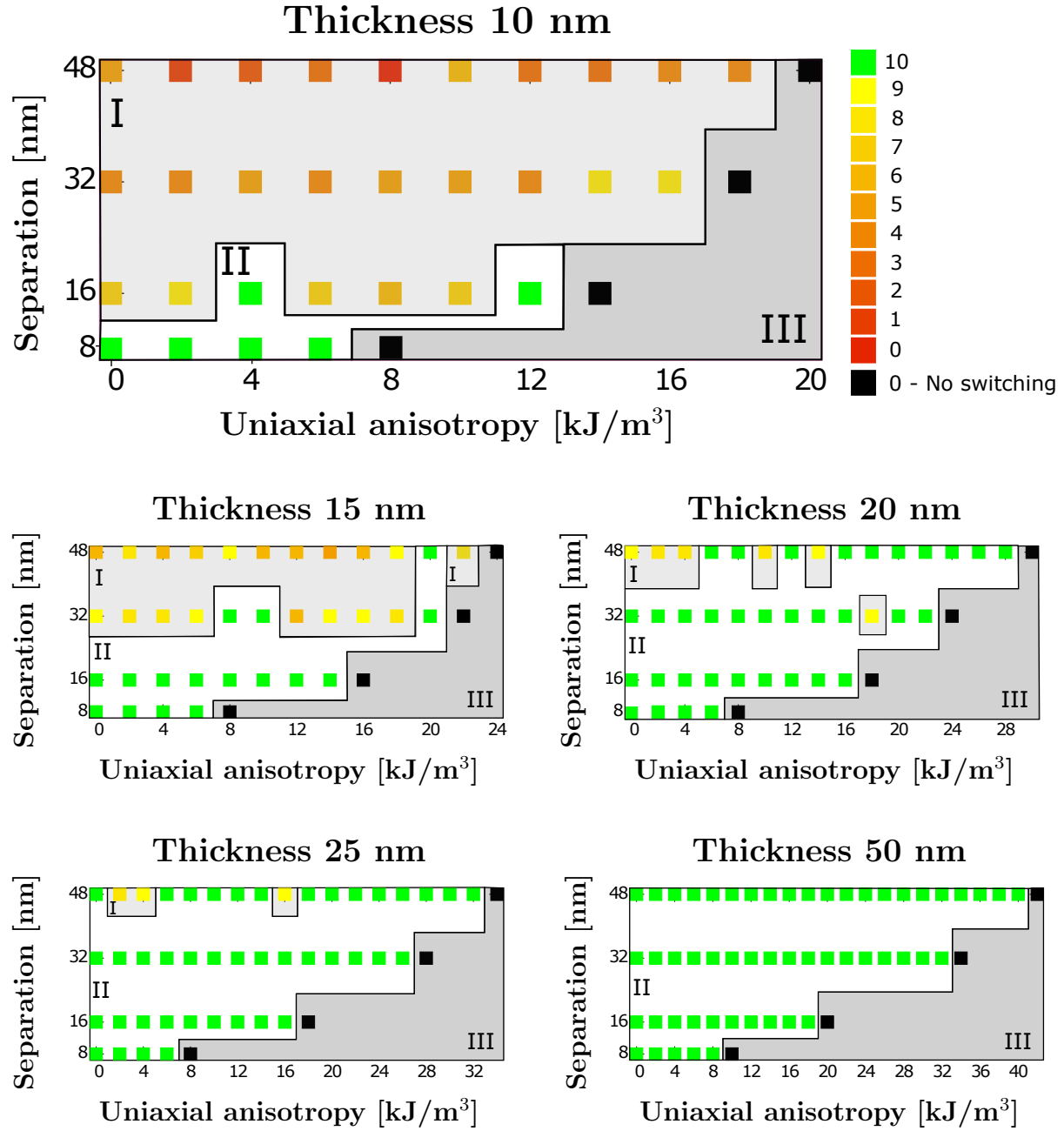


Figure 4.11: Results of 10 simulations per data point for thickness $t = 10$ nm, 15 nm, 20 nm, 25 nm and 50 nm. The variables are intermagnet spacing (separation) and uniaxial anisotropy.

As region II expands with increasing thickness, the expansion is more dominant in the right part of the figures, i.e., for higher uniaxial anisotropy values. This indicates that incorporating uniaxial anisotropy results in a higher success rate, given that the anisotropy is strong enough. Since the number of simulations per data point is limited to 10, and the step size for the uniaxial anisotropy is 2 kJ/m^3 , it would be beneficial to study the uniaxial anisotropy range just before cut-off more closely.

4.1.5 Findings for the nanomagnet chains

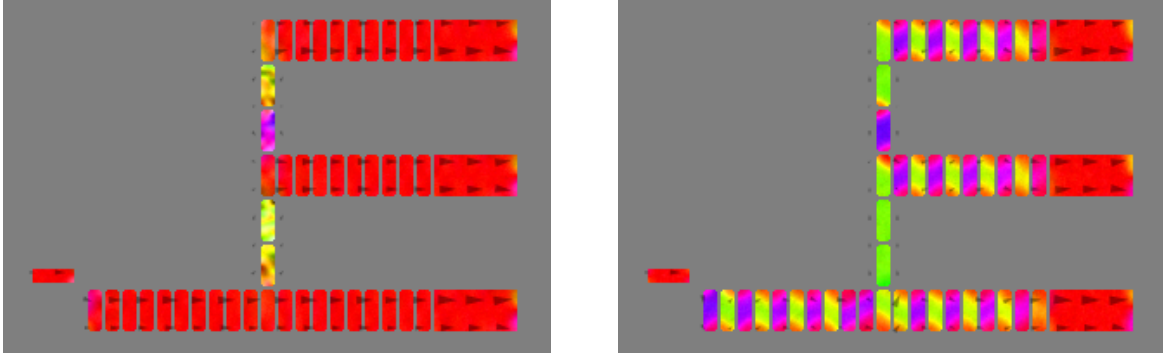
Three ways of increasing the success rates for nanomagnet chains have been identified; increasing the thickness, decreasing the intermagnet spacing and incorporating uniaxial anisotropy. Increasing the thickness has consistently proved to increase the success rates of NML systems, both in figure 4.4 and in the success rate plots of section 4.1.4. For a given thickness, decreasing the separation between the magnets has also shown to lead to more successful systems. The effect can be seen in both figures 4.6 and 4.7, in addition to the figures in section 4.1.4.

Section 4.1.4 confirmed that incorporating uniaxial anisotropy in the system can increase the success rate. The effect is most pronounced for large values of K_u in figure 4.11, for thicknesses $t = 10 \text{ nm}$ and $t = 15 \text{ nm}$. As the uniaxial anisotropy approaches the cut-off value, the success rates increase. For thickness $t > 15 \text{ nm}$, the systems display high success rates independent of uniaxial anisotropy.

In retrospect, seeing as the difference in success rate when adjusting the thickness or the intermagnet spacing is more pronounced than the aspect ratio tests, one might reconsider the choice of nanomagnet dimensions. Since the ultimate goal is use in logic devices, smaller is better. From the results obtained here, it would be interesting to see if a smaller aspect ratio can be compensated for by small adjustments to the thickness and/or intermagnet spacing.

4.2 Nanomagnet fanout structure

The results for the initial fanout structure is shown in figure 4.12. Before the start magnet could initiate the signal propagation, the magnetization of the vertical magnets started aligning along the easy axes, as seen in figure 4.12a. The final state of the fanout structure with the magnetic field turned off can be seen in figure 4.12b.



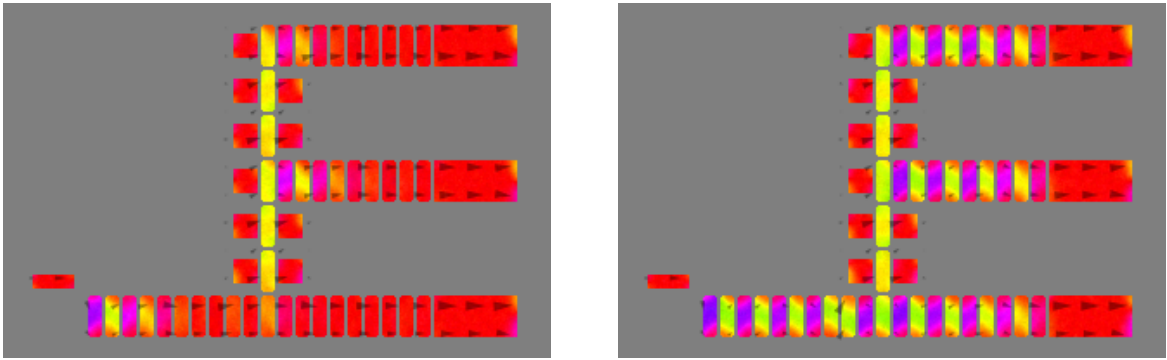
(a) At a magnetic field of 94 mT, the vertical magnets are no longer stable with magnetization in the +x-direction. (b) The fanout structure after the magnetic field has been turned off displaying unsuccessful propagation.

Figure 4.12: Two figures showing the fanout structure for (a) a magnetic field of 94 mT and (b) zero magnetic field.

The magnets in the horizontal chains, which are arranged with long-side to long-side, seem to be more stable than the vertical magnets which have their shortest sides facing each other. In figure 4.12a, the leftmost magnet in the top chain and the middle chain are more stable than the other vertical magnets, seen as they retain their magnetization closer to the initial hard axis stabilized state than the magnets which are not connected to other magnets horizontally. The final state, depicted in figure 4.12b, is a result of switching induced by the vertical magnets, not by the start magnet as intended.

A similar structure was studied by Carlton *et al.*, where signal propagation in NML systems of Co nanomagnets was investigated [25]. As Carlton's simulations were done by initializing the system with uniform magnetization in the +x-direction, an equivalent of removing the magnetic field abruptly, a simulation was done under these conditions. The result was similar to the scenario shown in figure 4.12, where premature switching of the vertical magnets resulted in unsuccessful propagation.

In order to stabilize the vertical chain and prohibit premature switching, additional magnets were added to the system. This approach was inspired by the aforementioned work of Carlton *et al.* Figure 4.13 shows the system at a magnetic field of 11 mT (4.13a) and at zero field (4.13b). The result of adding the stabilizing magnets was that the magnets in the vertical chain retained their magnetization along the shape anisotropy hard axis longer than without the use of stabilizing magnets. However, as was also the situation without stabilizer magnets, the magnets in the vertical chain underwent flipping of the magnetization before the signal from the start magnet had propagated to the vertical chain.



(a) At a magnetic field of 11 mT, the magnets in the vertical chain have all started changing their magnetization. (b) Figure showing the magnetization state of the NML system after removal of the magnetic field.

Figure 4.13: Figures showing a modified fanout structure where square magnets are situated close to the magnets in the vertical chain in an attempt to stabilize the system.

Comparing figure 4.12b and 4.13b, the magnetization directions of the magnets in the vertical chains differ. Where the initial system resulted in vertical magnets which had completely switched their magnetization to upwards magnetization, the same is not true for the system with stabilizing magnets along the vertical chain. It seems as though the presence of the stabilizing magnets hinders the vertical magnets from flipping to easy axis orientation, but that the stabilizing effect is not sufficient to obstruct signal propagation emerging from the vertical chain before the signal from the start magnet has propagated to the vertical chain.

The next step was to vary the geometry of the stabilizer magnets along the vertical chain in addition to the vertical intermagnet spacing in order to find some system parameters

which resulted in sufficiently stable magnets in the vertical chain, i.e., tuning the system parameters in such a way that the vertical magnets stayed magnetized in the $+x$ -direction until the signal from the start magnet had reached the vertical chain.

In order to keep the vertical chain magnets stable, the height of the stabilizer magnets was increased. Figure 4.14 illustrates a challenge which was encountered; when the height of the stabilizer magnets was relatively large (here, the maximal case of 192 nm, the same height as the chain magnets), the vertical chain magnets were more stable along the shape anisotropy hard axis, but the demagnetizing fields of the stabilizer magnets seem to flip the magnetization of the magnets in the horizontal chains. The dimensions of the square stabilizer magnets were tuned between the size in figure 4.13 and 4.14. However, no geometry was found which removed the problems of either not providing sufficient stability to the vertical chain or affecting the magnetization states of the magnets in the horizontal chains. The result was the same when changing the vertical intermagnet spacing.

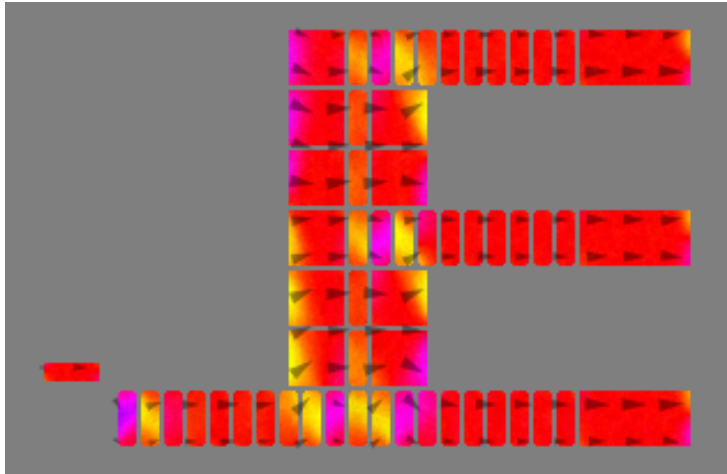


Figure 4.14: Illustration of the extreme case where the stabilizer magnets along the vertical chain have the same dimensions as the height of the chain magnets.

4.2.1 Findings for the fanout structure

When studying the fanout structure, controlling the magnets in the vertical chain proved difficult. Stabilizer magnets were incorporated in the system as an attempt to stabilize the chain magnets. The result was an increase in hard axis stability, however not sufficient to retain the magnetization of the vertical magnets until the signal from the start magnet had

propagated to the vertical chain. Parameter sets which prohibits the premature switching leading to unsuccessful propagation was not found.

The main takeaway from studying the fanout structure is that more investigation is needed on how to stabilize the vertical chain, before complex logic systems can be simulated with hope of successful results.

Chapter 5

Conclusions and Outlook

Micromagnetic simulations have been used to study LSMO nanomagnets for application in nanomagnetic logic. Most of the focus of this work has been put on investigating signal propagation in a chain of nanomagnets. The horizontally aligned chains consisted of 22 nanomagnets, with varying system parameters. In investigating the success rates of signal propagation, variables which results in successful propagation have been identified. Success rates can be increased by increasing the thickness of the magnets, decreasing the spacing or incorporating uniaxial anisotropy. The results also indicate that LSMO is a viable candidate for NML application.

Signal propagation was also explored for a more complex architecture, a fanout structure. This branched NML system included both horizontally and vertically aligned nanomagnet chains. The results of the simulations showed that tuning the system parameters in such a way that one can control the signal propagation in the vertical chains in addition to the horizontal chains is vital for making successful complex systems.

For future work a new simulation tool for NML is worth mentioning. ToPoliNano is designed specifically for simulating iNML systems. The tool simplifies the process of setting up NML systems using a top-down approach, and gives results on an architectural level [43]. Utilizing this tool in future projects has the potential to perform simulations more effectively and making the threshold lower for trying out a wide range of system setups.

The study of horizontal nanomagnet chains, together with an overview of the main challenges of making a larger NML system, provides a good foundation for a new project of which the starting point could be exploring how to control the stability of vertical chains in order to observe successful propagation in more complex NML systems.

Appendix A

Simulation Scripts

Listing A.1: Script for simulating a chain of nanomagnets

```
1 Temp = 100;
2 Thermseed(1);
3 Msat = 5.7e5; //saturation magnetization
4 Kc1 = 2100; //cubic anisotropy constant
5 alpha = 1.57e-3; //damping parameter
6 Aex = 1.4e-11; //exchange stiffness
7 anisC1 = vector(1,0,0); //easy axis along the x-direction
8 anisC2 = vector(0,1,0); //easy axis along the y-direction
9 FixDt = 1e-12;
10
11 //Uniaxial anisotropy
12 //anisU = vector(1,0,0); //easy axis for the uniaxial anisotropy
13 //Ku1 = 3000; //uniaxial anisotropy constant
14
15 snapshotformat = "png";
16 cellsizeXY := 8e-9;
17 antalMag := 22; //number of identical chain magnets
18 antalMag2 := floor(antalMag/2);
19
20 b := 64e-9; //island width
21 h := 192e-9; //island length
22 d := 32e-9; //intermagnet spacing
23 dStop := 32e-9; //spacing to stop magnet
24 dStartX := (b+d)*antalMag2 + h/2 + b/2 + 64e-9; //spacing to start
    magnet in x-direction
```

```

25 dStartY := h/2 + b/2 + 32e-9; //spacing to start magnet in y-direction
26 extraX := 40e-9;
27
28 nx := pow(2, ceil(log2( ( b*antalMag + d*(antalMag) + h + dStop + extraX ) /
    cellsizeXY ) )) ; //number of horizontal cells
29 ny := pow(2, ceil(log2( ( (h + b + dStartY) / cellsizeXY ) )) ) ; //number
    of vertical cells
30
31 SetMesh(nx, ny, 1, cellsizeXY, cellsizeXY, 20e-9, 0, 0, 0); //set up
    simulation environment
32
33 //Make magnets with rounded corners
34 r := 20e-9;
35 sq2 := rect(2*r, 2*r);
36 circ := circle(2*r);
37
38 rounded_ll := sq2.sub(circ).intersect(rect(r, r).transl(-r/2, -r/2, 0));
39 rounded_lr := sq2.sub(circ).intersect(rect(r, r).transl(r/2, -r/2, 0));
40 rounded_ul := sq2.sub(circ).intersect(rect(r, r).transl(-r/2, r/2, 0));
41 rounded_ur := sq2.sub(circ).intersect(rect(r, r).transl(r/2, r/2, 0));
42
43 //translated rounded corners
44 ll := rounded_ll.transl(-b/2+r, -h/2+r, 0);
45 lr := rounded_lr.transl(b/2-r, -h/2+r, 0);
46 ul := rounded_ul.transl(-b/2+r, h/2-r, 0);
47 ur := rounded_ur.transl(b/2-r, h/2-r, 0);
48
49 //island with sharp corners
50 sq := rect(b, h);
51 //rounding the corners
52 magnet := sq.sub(ll.add(lr).add(ul).add(ur));
53
54 arr := magnet;
55
56 for n := 1; n < antalMag2; n++{
57     arr = arr.add(magnet.transl((b+d)*n, 0, 0));
58 }
59 for n := 1; n <= antalMag2; n++{
60     arr = arr.add(magnet.transl(-(b+d)*n, 0, 0));
61 }
62

```

```

63 //start magnet
64 startMagnet := rect(h,b);
65 arr = arr.add(startMagnet.transl(-dStartX, dStartY,0));
66
67 //stop magnet
68 stoppMagnet := rect(2*h,h);
69 arr = arr.add(stoppMagnet.transl((b+d)*(antalMag2-1) + h + b/2 + dStop,0,0))
70 ;
71 SetGeom(arr);
72
73 tableadd(B_ext);
74 m = uniform(1,0,0);
75
76 Bx := 0.12;
77 B_ext = vector(Bx, 0, 0); //magnetic field
78 rampStep := 0.001;
79
80 for Bx >= 0.048{
81     run(1e-9);
82     snapshot(m);
83     save(m);
84     tablesave();
85     Bx -= rampStep;
86     B_ext = vector(Bx,0,0);
87 }

```

Listing A.2: Script for simulating a fanout structure

```

1 Temp = 100;
2 Msat = 5.7e5;
3 Kc1 = 2100;
4 Thermseed(1);
5 alpha = 1.57e-3;
6 Aex = 1.4e-11;
7 anisC1 = vector(1,0,0);
8 anisC2 = vector(0,1,0);
9 FixDt = 1e-12;
10
11 //Uniaxial anisotropy
12 anisU = vector(1,0,0);
13 Ku1 = 18000;

```

```

14
15 snapshotformat = "png";
16 cellsizeXY := 8e-9;
17 antalMagLong := 21;      //longest chain
18 antalMag2 := floor(antalMagLong/2);
19 antalMagY := 7;          //number of vertical magnets
20 antalMagY2 := floor(antalMagY/2);
21
22 b := 64e-9;              //island width
23 h := 192e-9;             //island length
24 d := 16e-9;              //horizontal intermagnet spacing
25 dVert := 2*d;            //vertical intermagnet spacing
26 dStop := 16e-9;          //spacing to stop magnet
27 dStartX := (b+d)*antalMag2 + h/2 + b/2 + 64e-9; //spacing to start magnet
    in x-direction
28 dStartY := h/2 + b/2 + 32e-9;
29 extraX := 0e-9;
30
31 nx := pow(2, ceil(log2( ( (b+d)*antalMagLong + 3*h + dStop + extraX ) /
    cellsizeXY ) ) ) ;
32 ny := pow(2, ceil(log2( ( (h + b)*antalMagY / cellsizeXY ) ) ) ) ;
33
34 SetMesh(nx, ny, 1, cellsizeXY, cellsizeXY, 50e-9, 0, 0, 0);
35
36 //Rounded corners
37 r := 20e-9;
38 sq2 := rect(2*r,2*r);
39 circ:= circle(2*r);
40
41 rounded_ll := sq2.sub(circ).intersect(rect(r,r).transl(-r/2,-r/2,0));
42 rounded_lr := sq2.sub(circ).intersect(rect(r,r).transl(r/2,-r/2,0));
43 rounded_ul := sq2.sub(circ).intersect(rect(r,r).transl(-r/2,r/2,0));
44 rounded_ur := sq2.sub(circ).intersect(rect(r,r).transl(r/2,r/2,0));
45
46 //translated rounded corners
47 ll := rounded_ll.transl(-b/2+r,-h/2+r,0);
48 lr := rounded_lr.transl(b/2-r,-h/2+r,0);
49 ul := rounded_ul.transl(-b/2+r,h/2-r,0);
50 ur := rounded_ur.transl(b/2-r,h/2-r,0);
51
52 //island with sharp corners

```



```

53 sq := rect(b,h);
54 //rounding the corners
55 magnet := sq.sub( ll.add(lr).add(ul).add(ur));
56
57 arr := magnet.transl(0,-antalMagY2*(h+dVert),0);
58
59 //add magnets to the chain
60 for n := 1; n < antalMag2; n++){
61     arr = arr.add(magnet.transl((b+d)*n,-antalMagY2*(h+dVert),0));
62     arr = arr.add(magnet.transl((b+d)*n,antalMagY2*(h+dVert),0));
63     arr = arr.add(magnet.transl((b+d)*n,0,0));
64 }
65 for n := 1; n <= antalMag2; n++){
66     arr = arr.add(magnet.transl(-(b+d)*n,-antalMagY2*(h+dVert),0));
67 }
68
69 //start magnet
70 startMagnet := rect(h,b);
71 arr = arr.add(startMagnet.transl(-dStartX, dStartY - antalMagY2*(h+dVert),0)
    );
72
73 //fanoutY
74 bStabX := 1.8*b;
75 bStabY := 1.8*b;
76 stabMag := rect(bStabX,bStabY);
77 for y := 1; y < antalMagY; y++){
78     arr = arr.add(magnet.transl(0, -(h+dVert)*antalMagY2 + (h+dVert)*y,0));
79     arr = arr.add(stabMag.transl(-(bStabX/2 + d + b/2), -(h+dVert)*antalMagY2
    + (h+dVert)*y, 0));
80     if !(mod(y,3) == 0){
81         arr = arr.add(stabMag.transl((bStabX/2 + d + b/2), -(h+dVert)*
    antalMagY2 + (h+dVert)*y, 0));
82     }
83 }
84
85 //stop magnet
86 stoppMagnet := rect(2*h,h);
87 arr = arr.add(stoppMagnet.transl((b+d)*(antalMag2-1) + h + b/2 + dStop,0,0)
    );
88 arr = arr.add(stoppMagnet.transl((b+d)*(antalMag2-1) + h + b/2 + dStop, (h+
    dVert)*antalMagY2,0));

```

```

89 arr = arr.add(stoppMagnet.transl((b+d)*(antalMag2-1) + h + b/2 + dStop, -(h+
    dVert)*antalMagY2, 0));
90
91 SetGeom(arr);
92 snapshot(m);
93 tableadd(B_ext);
94 m = uniform(1,0,0);
95
96 Bx := 0.094;
97 B_ext = vector(Bx, 0, 0);
98
99 rampStep := 0.001;
100
101 for Bx >= 0.0{
102     run(1e-9);
103     snapshot(m);
104     save(m);
105     tablesave();
106     Bx -= rampStep;
107     B_ext = vector(Bx,0,0);
108 }

```

References

- [1] Intel Corporation. *Moore's Law and Intel Innovation*. URL: <https://www.intel.com/content/www/us/en/history/museum-gordon-moore-law.html> (visited on 12/27/2017).
- [2] Intel Corporation. *50 Years of Moore's Law*. URL: <https://www.intel.com/content/www/us/en/silicon-innovations/moores-law-technology.html> (visited on 12/27/2017).
- [3] SemiAccurate. *What is the state of Intel's 10nm process?* 2017. URL: <https://semiaccurate.com/2017/12/20/state-intels-10nm-process/> (visited on 01/05/2018).
- [4] Ars Technica. *Moore's law really is dead this time*. 2016. URL: <https://arstechnica.com/information-technology/2016/02/moores-law-really-is-dead-this-time/> (visited on 01/05/2018).
- [5] MIT Technology Review. *Intel: Chips Will Have to Sacrifice Speed Gains for Energy Savings*. 2016. URL: <https://www.technologyreview.com/s/600716/intel-chips-will-have-to-sacrifice-speed-gains-for-energy-savings/> (visited on 01/05/2018).
- [6] Niemier, M. T. et al. "Nanomagnet logic: progress toward system-level integration". *Journal of Physics: Condensed Matter*, 23(49): p. 493202, 2011.
- [7] Imre, A. et al. "Majority Logic Gate for Magnetic Quantum-Dot Cellular Automata". *Science*, 311(5758): pp. 205–208, 2006. ISSN: 0036-8075. DOI: 10.1126/science.1120506.

- [8] Gu, Z. et al. “Sub-nanosecond signal propagation in anisotropy engineered nano-magnetic logic chains”. *Nature Communications*, 2014. DOI: 10.1038/ncomms7466.
- [9] Zhang, B. et al. “Innovative orderly programmable in-plane majority gates using trapezoid shape nanomagnet logic devices”. *Micro & Nano Letters*, 9(5): pp. 359–362, 2014.
- [10] Varga, E. et al. “Experimental Demonstration of Fanout for Nanomagnetic Logic”. *IEEE Transactions on Nanotechnology*, 9(6): pp. 668–670, 2010. ISSN: 1536-125X. DOI: 10.1109/TNANO.2010.2060347.
- [11] Yang, X. et al. “Micromagnetic simulation of exploratory magnetic logic device with missing corner defect”. *Journal of Magnetism and Magnetic Materials*, 394, pp. 391–396, 2015. ISSN: 0304-8853. DOI: <http://dx.doi.org/10.1016/j.jmmm.2015.06.068>.
- [12] I. Hallsteinsen et al. “Crystalline symmetry controlled magnetic switching in epitaxial (111) $\text{La}_{0.7}\text{Sr}_{0.3}\text{MnO}_3$ thin films”. *Citation: APL Materials Journal of Applied Physics*, 31(10): 2015. DOI: 10.1063/1.4907877.
- [13] Takamura, Y. et al. “Spin-Flop Coupling and Exchange Bias in Embedded Complex Oxide Micromagnets”. *Phys. Rev. Lett.* 111, p. 107201, 10 2013. DOI: 10.1103/PhysRevLett.111.107201.
- [14] Boschker, J. E. et al. “Consequences of High Adatom Energy during Pulsed Laser Deposition of $\text{La}_{0.7}\text{Sr}_{0.3}\text{MnO}_3$ ”. *Crystal Growth & Design*, 12(2): pp. 562–566, 2012. DOI: 10.1021/cg201461a.
- [15] Vansteenkiste, A. et al. “The design and verification of MuMax3”. *AIP Advances*, 4(10): pp. 1–32, 2014. ISSN: 21583226. DOI: 10.1063/1.4899186.
- [16] Krishnan, K. M. *Fundamentals and Applications of Magnetic Materials*. Oxford University Press, 2016.

- [17] Skomski, R. “Curie temperature and density of states of quasi-weak ferromagnets”. *Journal of Magnetism and Magnetic Materials*, 140-144(Part 3): pp. 2003–2004, 1995. ISSN: 0304-8853. DOI: [https://doi.org/10.1016/0304-8853\(94\)00700-4](https://doi.org/10.1016/0304-8853(94)00700-4).
- [18] Visintin, A. “On Landau-Lifshitz’ equations for ferromagnetism”. *Japan Journal of Applied Mathematics*, 2(1): p. 69, 1985. ISSN: 0910-2043. DOI: 10.1007/BF03167039.
- [19] Landau, L. and Lifshitz, E. “On the theory of the dispersion of magnetic permeability in ferromagnetic bodies”. *Phys. Z. Sowjetunion*, 8(153): pp. 101–114, 1935.
- [20] Brown, W. *Micromagnetics*. John Wiley & Sons, Inc. Interscience Publishers, 1963.
- [21] Brown, W. “Domains, micromagnetics, and beyond: Reminiscences and assessments”. *Journal of Applied Physics*, 49(3): pp. 1937–1942, 1978. DOI: 10.1063/1.324811.
- [22] Abo, G. et al. “Definition of magnetic exchange length”. *IEEE Transactions on Magnetics*, 49(8): pp. 4937–4939, 2013. ISSN: 00189464. DOI: 10.1109/TMAG.2013.2258028.
- [23] Hornyak, G. L. *Introduction to nanoscience & nanotechnology*. CRC Press, 2009.
- [24] Cowburn, R. P. “Probing antiferromagnetic coupling between nanomagnets”. *Phys. Rev. B*, 65, p. 092409, 9 2002. DOI: 10.1103/PhysRevB.65.092409.
- [25] Carlton, D. B. et al. “Simulation Studies of Nanomagnet-Based Logic Architecture”. *Nano Letters*, 8(12): pp. 4173–4178, 2008. DOI: 10.1021/nl801607p.
- [26] Csaba, G., Lugli, P., and Porod, W. “Power dissipation in nanomagnetic logic devices”. *4th IEEE Conference on Nanotechnology, 2004*. 2004, pp. 346–348. DOI: 10.1109/NANO.2004.1392346.
- [27] Carlton, D. B. et al. “Investigation of Defects and Errors in Nanomagnetic Logic Circuits”. *IEEE Transactions on Nanotechnology*, 11(4): pp. 760–762, 2012. ISSN: 1536-125X. DOI: 10.1109/TNANO.2012.2196445.

- [28] Imre, A. et al. “Investigation of shape-dependent switching of coupled nanomagnets”. *Superlattices and Microstructures*, 34(3): pp. 513–518, 2003. ISSN: 0749-6036. DOI: <http://dx.doi.org/10.1016/j.spmi.2004.03.051>.
- [29] Niemier, M. T. et al. “Shape Engineering for Controlled Switching With Nanomagnet Logic”. *IEEE Transactions on Nanotechnology*, 11(2): pp. 220–230, 2012. ISSN: 1536-125X. DOI: 10.1109/TNANO.2010.2056697.
- [30] Lambson, B. et al. “Cascade-like signal propagation in chains of concave nanomagnets”. *Applied Physics Letters*, 100(15): p. 152406, 2012. DOI: 10.1063/1.3703591.
- [31] Lambson, B. et al. “Concave nanomagnets: investigation of anisotropy properties and applications to nanomagnetic logic”. *Applied Physics A*, 111(2): pp. 413–421, 2013. ISSN: 1432-0630. DOI: 10.1007/s00339-013-7654-y.
- [32] Shah, F. A. et al. “Error analysis for ultra dense nanomagnet logic circuits”. *Journal of Applied Physics*, 117(17): 17A906, 2015. DOI: 10.1063/1.4915353.
- [33] Perna, P. et al. “Tailoring magnetic anisotropy in epitaxial half metallic $\text{La}_{0.7}\text{Sr}_{0.3}\text{MnO}_3$ thin films”. *Journal of Applied Physics*, 110(1): p. 013919, 2011. DOI: 10.1063/1.3605542.
- [34] Niemier, M. “Magnetic devices: Clocking with no field”. *Nature Nanotechnology*, 9(1): pp. 14–5, 2014.
- [35] Puliafito, V. et al. “Nanomagnetic logic with non-uniform states of clocking”. *Journal of Physics D: Applied Physics*, 49(14): p. 145001, 2016.
- [36] Munira, K. et al. “Reducing error rates in straintronic multiferroic nanomagnetic logic by pulse shaping”. *Nanotechnology*, 26(24): p. 245202, 2015.
- [37] Steenbeck, K. and Hiergeist, R. “Magnetic anisotropy of ferromagnetic $\text{La}_{0.7}\text{Sr}_{0.3}\text{MnO}_3$ epitaxial films”. *Applied Physics Letters*, 75(12): pp. 1778–1780, 1999. DOI: 10.1063/1.124817.

- [38] Hubert, A. and Schäfer, R. *Magnetic Domains: The Analysis of Magnetic Microstructures*. Springer, 1998. ISBN: 9783540641087.
- [39] Lee, M. S. et al. “Tailoring Spin Textures in Complex Oxide Micromagnets”. *ACS Nano*, 10(9): pp. 8545–8551, 2016. DOI: 10.1021/acsnano.6b03770.
- [40] Lee, H. H. *Micromagnetic modelling of thermally induced errors in nanomagnetic logic*. Specialization project report. Trondheim, Norway, 2017.
- [41] Luo, G. Y. et al. “Enhanced magnetic damping in $\text{La}_{0.7}\text{Sr}_{0.3}\text{MnO}_3$ capped by normal metal layer”. *AIP Advances*, 5(9): p. 097148, 2015. DOI: 10.1063/1.4931383.
- [42] Folven, E. et al. “Controlling the switching field in nanomagnets by means of domain-engineered antiferromagnets”. *Phys. Rev. B*, 92, p. 094421, 9 2015. DOI: 10.1103/PhysRevB.92.094421.
- [43] Riente, F. et al. “ToPoliNano: A CAD Tool for Nano Magnetic Logic”. *IEEE Transactions on Computer-Aided Design of Integrated Circuits and Systems*, 36(7): pp. 1061–1074, 2017. ISSN: 0278-0070. DOI: 10.1109/TCAD.2017.2650983.